

## INSIGHT INTO THE FORMATION OF THE MILKY WAY THROUGH COLD HALO SUBSTRUCTURE. II. THE ELEMENTAL ABUNDANCES OF ECHOS

KEVIN C. SCHLAUFMAN<sup>1,5</sup>, CONSTANCE M. ROCKOSI<sup>1,6,7</sup>, YOUNG SUN LEE<sup>2</sup>, TIMOTHY C. BEERS<sup>2</sup>, AND CARLOS ALLENDE PRIETO<sup>3,4</sup>

*Received 2010 July 29; accepted 2011 April 3*

### ABSTRACT

We determine the average metallicities of the elements of cold halo substructure (ECHOS) that we previously identified in the inner halo of the Milky Way within 17.5 kpc of the Sun. As a population, we find that stars kinematically associated with ECHOS are chemically distinct from the background kinematically smooth inner halo stellar population along the same Sloan Extension for Galactic Understanding and Exploration (SEGUE) line of sight. ECHOS are systematically more iron-rich, but less  $\alpha$ -enhanced than the kinematically-smooth component of the inner halo. ECHOS are also chemically distinct from other Milky Way components: more iron-poor than typical thick-disk stars and both more iron-poor and  $\alpha$ -enhanced than typical thin-disk stars. In addition, the radial velocity dispersion distribution of ECHOS extends beyond  $\sigma \sim 20 \text{ km s}^{-1}$ . Globular clusters are unlikely ECHOS progenitors, as ECHOS have large velocity dispersions and are found in a region of the Galaxy in which iron-rich globular clusters are very rare. Likewise, the chemical composition of stars in ECHOS do not match predictions for stars formed in the Milky Way and subsequently scattered into the inner halo. Dwarf spheroidal (dSph) galaxies are possible ECHOS progenitors, and if ECHOS are formed through the tidal disruption of one or more dSph galaxies, the typical ECHOS  $[\text{Fe}/\text{H}] \sim -1.0$  and radial velocity dispersion  $\sigma \sim 20 \text{ km s}^{-1}$  implies a dSph with  $M_{\text{tot}} \gtrsim 10^9 M_{\odot}$ . Our observations confirm the predictions of theoretical models of Milky Way halo formation that suggest that prominent substructures are likely to be metal-rich, and our result implies that the most likely metallicity for a recently accreted star currently in the inner halo is  $[\text{Fe}/\text{H}] \sim -1.0$ .

*Subject headings:* Galaxy: abundances — Galaxy: formation — Galaxy: halo — Galaxy: kinematics and dynamics

### 1. INTRODUCTION

In  $\Lambda$ CDM cosmology, galaxies like the Milky Way are formed through the stochastic accretion of smaller dark matter halos and the continuous accretion of gas (e.g., Press & Schechter 1974; White & Rees 1978). The statistical properties of the stochastic accretion have been well characterized by large cosmological dark matter only  $n$ -body simulations (e.g., Springel et al. 2005). On the other hand, no model has yet self-consistently incorporated the gas dynamics, star formation, and feedback necessary to satisfactorily reproduce the formation of Milky Way analogs. In any case, an understanding of the statistical properties of the accretion histories of Milky Way analogs does not predict the unique formation history of the Milky Way. Fortunately, the dynamical and chemical properties of the Milky Way's thin disk, thick disk, bulge, and halo provide strong constraints on the formation of our own Galaxy (e.g.,

Freeman & Bland-Hawthorn 2002; Helmi 2008).

The kinematics of the stellar halo of the Milky Way are simpler to describe than the kinematics of other Galactic components. As a result, the stellar halo is the Galactic component in which it is easiest to unambiguously identify the remnants of the smaller halos that the Milky Way has accreted through its history. For that reason, the substructures recently discovered in the halo provide a direct measure of accretion in the region of the Galaxy that is far easier to model than the disk or the bulge. The existence of substructure in the halo of the Milky Way is now well established by star counts (e.g., Totten & Irwin 1998; Totten et al. 2000; Ivezić et al. 2000; Yanny et al. 2000; Odenkirchen et al. 2001; Vivas et al. 2001; Gilmore et al. 2002; Newberg et al. 2002; Rockosi et al. 2002; Majewski et al. 2003; Yanny et al. 2003; Rocha-Pinto et al. 2004; Duffau et al. 2006; Belokurov et al. 2006; Grillmair & Johnson 2006; Grillmair & Dionatos 2006; Vivas & Zinn 2006; Belokurov et al. 2007; Bell et al. 2008; Jurić et al. 2008; Grillmair 2009; Watkins et al. 2009), kinematic measurements (e.g., Majewski et al. 1996; Chiba & Yoshii 1998; Helmi et al. 1999; Chiba & Beers 2000; Kepley et al. 2007; Ivezić et al. 2008; Klement et al. 2008; Seabroke et al. 2008; Klement et al. 2009; Smith et al. 2009; Starkenburg et al. 2009), and chemical abundances (e.g., Ivezić et al. 2008; An et al. 2009); these observed substructures are likely the remains of the stellar populations that formed as part of independent, bound structures that are now being disrupted and

<sup>1</sup> Astronomy and Astrophysics Department, University of California, Santa Cruz, CA 95064, USA; kcs@ucolick.org and crockosi@ucolick.org

<sup>2</sup> Dept. of Physics and Astronomy and JINA: Joint Institute for Nuclear Astrophysics, Michigan State University, E. Lansing, MI 48824, USA; lee@pa.msu.edu and beers@pa.msu.edu

<sup>3</sup> Instituto de Astrofísica de Canarias, 38205 La Laguna, Tenerife, Spain; callende@iac.es

<sup>4</sup> Departamento de Astrofísica, Universidad de La Laguna, 38206 La Laguna, Tenerife, Spain

<sup>5</sup> NSF Graduate Research Fellow

<sup>6</sup> University of California Observatories

<sup>7</sup> Packard Fellow

dispersed in the halo.

In the first paper in this series, Schlaufman et al. (2009)–S09 hereafter—we identified elements of cold halo substructure (ECHOS) as overdensities in the spatial and radial velocity distribution of the inner halo’s stellar population. Except for those ECHOS identified along lines of sight known to host surface brightness substructure, none of our ECHOS are detected as overdensities of stars in surface brightness substructure. As a result, they are distinct from surface brightness substructure and are likely the debris of more ancient accretion events. We used our detections to infer that as much as 10% of the inner halo by volume might have 30% of its stars in ECHOS, and we used that measurement together with similar measurements for surface brightness substructure to suggest that the Milky Way’s accretion history has been roughly constant over the last few Gyr with no massive ( $M_{\text{tot}} \sim 10^{10} M_{\odot}$ ) single accretion events in that interval. Moreover, the distribution of ECHOS in Galactic coordinates is consistent with isotropy given the completeness limits of our search, possibly indicating an accretion origin for ECHOS (rather than an association with the Galactic disk).

The chemical composition of the Milky Way’s stellar populations also illuminate their origin (e.g., McWilliam 1997). In general, since iron is introduced into the interstellar medium in supernovae (SN) explosions, the  $[\text{Fe}/\text{H}]$  of a stellar population is correlated with the total integrated star formation that occurred in that population. Qualitatively then, low  $[\text{Fe}/\text{H}]$  indicates relatively little integrated star formation, while high  $[\text{Fe}/\text{H}]$  indicates relatively more integrated star formation. If the initial mass function (IMF) of stellar populations is not a strong function of environment or metallicity at  $[\text{Fe}/\text{H}] \gtrsim -3.0$  (e.g., Bastian et al. 2010), then a stellar population’s abundances of the  $\alpha$ -elements (O, Mg, Si, Ca, and Ti) relative to iron are related to the duration of the star formation that produced that population. Core-collapse (i.e., Type II and Type Ibc) SN result from the explosions of stars initially more massive than about  $8 M_{\odot}$  and produce large amounts of the  $\alpha$ -elements relative to iron. Since stars that massive spend very little time on the main sequence, the enrichment of the interstellar medium (ISM) by the ejecta from core-collapse SN occurs very quickly, within a few Myr. In contrast, thermonuclear (i.e., Type Ia) SN result from the explosion of white dwarfs as a result of runaway nuclear burning and produce large amounts of iron relative to the  $\alpha$ -elements. The exact progenitor and therefore the characteristic timescale on which thermonuclear SN start to enrich the ISM is still debated (e.g., Scannapieco & Bildsten 2005); nevertheless, the timescale is longer than the comparable time to ISM enrichment through core-collapse SN. For those reasons, a short burst of star formation will leave behind a stellar population with  $[\alpha/\text{Fe}] \gtrsim 0$ , while a more extended star formation history will produce a population with  $[\alpha/\text{Fe}] \sim 0$  (neglecting any differences in the IMF). Accordingly, a lower star formation rate will allow thermonuclear SN to reduce  $[\alpha/\text{Fe}]$  at relatively low  $[\text{Fe}/\text{H}]$ , whereas a high star formation rate will produce many generations of stars before thermonuclear SN begin to reduce  $[\alpha/\text{Fe}]$ , pushing the “knee” in the  $[\text{Fe}/\text{H}]$ – $[\alpha/\text{Fe}]$  plane to higher  $[\text{Fe}/\text{H}]$ .

Stars in the inner halo typically have  $[\text{Fe}/\text{H}] \sim -1.6$

and are enhanced in the  $\alpha$ -elements relative to iron (e.g., Ryan & Norris 1991a,b; McWilliam et al. 1995; Allende Prieto et al. 2006). Robertson et al. (2005) explained the chemistry of most of the stellar mass in the inner halo in the context of the  $\Lambda\text{CDM}$  model of galaxy formation with the accretion of a massive  $M_{\text{tot}} \sim 5 \times 10^{10} M_{\odot}$  halo  $\sim 10$  Gyr in the past. The high-mass and short-timescale for star formation in such a massive progenitor of the inner halo are consistent with the observed chemistry. This scenario is in contrast to the composition of the classical dwarf spheroidal galaxies (dSph), which at the average  $[\text{Fe}/\text{H}]$  of the inner halo have  $[\alpha/\text{Fe}]$  closer to solar (e.g., Mateo 1998). At the same time, the Robertson et al. (2005) model did not directly address the origin of the substructure now known to exist in the inner halo, and those substructures are likely related to more recent accretion events.

In the same way, the chemical properties of substructure reveal something about its origin. Since ECHOS are likely the remains of recent accretion events ( $\tau \lesssim 5$  Gyr), their chemical composition constrains the properties of a more recently-disrupted class of contributors to the stellar population of the inner halo than the few massive progenitors that contributed the bulk of the inner halo’s stellar population. If ECHOS are the remains of disrupted dSph galaxies, then the dSph luminosity–metallicity relation can be used to infer the luminosity of a progenitor from its mean iron metallicity (e.g., Helmi et al. 2006b; Kirby et al. 2008b). Indeed, the Kirby et al. (2008b) luminosity–metallicity relation for dSph galaxies is now well calibrated over four decades in luminosity using. Combined with stellar mass to light ratios, the Kirby et al. (2008b) luminosity–metallicity relation can be turned into a stellar mass–metallicity relation. As a result, the average iron metallicity of a dSph stellar population can be considered a proxy for its stellar mass. Likewise, the  $[\alpha/\text{Fe}]$  of substructure indicates the duration of star formation in its progenitor. Typical halo stars have  $[\alpha/\text{Fe}] \gtrsim 0.3$  at  $[\text{Fe}/\text{H}] \sim -1.6$  indicating formation in a truncated episode of star formation. In contrast, stars in classical dSph typical have  $[\alpha/\text{Fe}] \sim 0$  at  $[\text{Fe}/\text{H}] \sim -1.6$ , indicating formation in an episode of prolonged star formation.

We measure the chemical properties of the ECHOS discovered in S09 and use their combined kinematic and dynamical properties to better understand their origin in the context of the  $\Lambda\text{CDM}$  model of Galaxy formation. This paper is organized as follows: in Section 2 we describe the data we use in this analysis. In Section 3 we describe how we derive average  $[\text{Fe}/\text{H}]$  and  $[\alpha/\text{Fe}]$  for each ECHOS through the analysis of coadded metal-poor main sequence turnoff star spectra creating using spectra from individual metal-poor main sequence turnoff stars kinematically associated with each ECHOS. In Section 4 we discuss the implications of our findings for the formation of the Milky Way. We summarize our conclusions in Section 5.

## 2. DATA

The Sloan Extension for Galactic Understanding and Exploration (SEGUE) survey observed approximately 240,000 Milky Way stars with apparent magnitudes in the range  $14 < g < 20.3$  with the fiber-fed Sloan Digital Sky Survey (SDSS) spectrograph at moderate resolution.

Spectroscopic targets were selected from the combined  $11,663 \text{ deg}^2$   $ugriz$  photometric footprint of the SDSS and SEGUE. The SDSS telescope and spectrograph obtain  $R \approx 1800$  spectra between  $3900 \text{ \AA}$  and  $9000 \text{ \AA}$  with high spectrophotometric accuracy. The SEGUE instrumentation, data processing pipelines, survey strategy, along with radial velocity and atmospheric parameter accuracies are described in Yanny et al. (2009), Lee et al. (2008a,b), Allende Prieto et al. (2008), and the SDSS-II DR7 paper (Abazajian et al. 2009). The SDSS survey is described in detail in Fukugita et al. (1996), Gunn et al. (1998), York et al. (2000), Hogg et al. (2001), Smith et al. (2002), Pier et al. (2003), Ivezić et al. (2004), Gunn et al. (2006), Tucker et al. (2006), and Padmanabhan et al. (2008).

In S09 we examined a sample of 10,739 metal-poor main sequence turnoff stars collected from 137 seven  $\text{deg}^2$  lines of sight. These metal-poor main sequence turnoff (MPMSTO) stars have both the  $g - r$  color and significant UV excess expected for the main sequence turnoff of a metal-poor population (for a detailed description of the MPMSTO sample see Section 2 of S09). Given the magnitude limits of the SEGUE survey, the MPMSTO sample was selected because MPMSTO stars are the highest-density tracer of the inner halo. In S09, we defined the inner halo as the volume more than 10 kpc from the Galactic center, within 17.5 kpc of the Sun, and more than 4 kpc from the Galactic plane. Though we found no reason to reject a kinematically smooth model for the inner halo on average, we discovered many radial velocity overdensities that we termed ECHOS. We identified ECHOS along individual lines of sight along which there was a very significant deviation from a kinematically smooth model of the inner halo. We gave these substructure the name ECHOS to differentiate them from surface brightness substructure like tidal streams, as the only ECHOS we could relate to surface brightness substructures were those ECHOS discovered along lines of sight targeted at known surface brightness substructures. ECHOS are also distinct in that they are likely related to more ancient accretion events than surface brightness substructure in the same volume (e.g., Johnston et al. 2008). As the same time, ECHOS are likely related to more recent accretion events than those substructures that will be discovered in the same volume using the 6D kinematic data that will become available from Gaia and the LSST (e.g., Helmi et al. 2006a; McMillan & Binney 2008; Gómez & Helmi 2010). The ECHOS we discovered were preferentially bunched at the faintest apparent magnitudes of the SEGUE spectroscopic sample; indeed the 25%, 50%, and 75% percentile in  $r$ -magnitude and spectral signal to noise per  $1 \text{ \AA}$  pixel (abbreviated S/N hereafter) were (19.0, 19.5, 19.8) and (7.6, 10.4, 15.4) respectively. As a result, the spectra of individual MPMSTO stars were generally at too low a S/N to precisely measure abundances.

### 3. ANALYSIS

We coadd all stellar spectra kinematically associated with an ECHOS in a narrow range of effective temperature and analyze the resultant coadded spectrum to determine the average abundance of the ECHOS. At the same time, we use an equivalent coaddition process to

determine the average metallicity of the MPMSTO stars in the kinematically smooth inner halo population along the same line of sight.

We use these measurements to compare the mean chemical abundance of the ECHOS and smooth halo population. Both calculations are subject to the same systematics, so any apparent chemical offset can only result from an underlying chemical difference or from random effects. To quantify the effects of randomness, we compute the precision and accuracy of our technique by analyzing two classes of objects with known composition. The first class of objects are individual MPMSTO stars that have been observed both at high S/N during the SEGUE survey and at high resolution by larger telescopes. The high S/N SEGUE spectra can be degraded to arbitrarily low S/N by a detailed noise model so that we can test the coaddition process with data representative of the low S/N spectra available for MPMSTO stars in ECHOS. The second class of objects are MPMSTO stars associated with the globular clusters M 13 and M 15. Using those two test cases, we quantify the mean square error ( $\text{MSE} \equiv \text{bias}^2 + \text{variance}$ ) of our metallicity estimates. We describe these steps in detail in the following subsections.

#### 3.1. The SEGUE Stellar Parameter Pipeline

The SEGUE Stellar Parameter Pipeline (SSPP - Lee et al. 2008a,b; Allende Prieto et al. 2008) uses Sloan spectroscopy and  $ugriz$  photometry to infer the stellar atmosphere parameters ( $T_{\text{eff}}$ ,  $\log g$ ,  $[\text{Fe}/\text{H}]$ , and  $[\alpha/\text{Fe}]$ ) of stars observed in the course of SDSS and SEGUE. The SSPP implements a multimethod algorithm in which many different techniques are used to compute the stellar parameters. The SSPP then averages the result of each method known to be valid in a given color and S/N range to determine the final  $T_{\text{eff}}$ ,  $\log g$ ,  $[\text{Fe}/\text{H}]$ , and  $[\alpha/\text{Fe}]$  reported for all stars observed in the SDSS and SEGUE surveys.

Lee et al. (2008a,b) determined the accuracy and precision of the SSPP in three ways. First, they compared the atmospheric parameters determined by the SSPP from high S/N SEGUE spectra with the atmospheric parameters determined from high-resolution spectroscopy from HIRES and ESI on the Keck Telescopes, HRS on the Hobby-Eberly Telescope (HET), and HDS on the Subaru Telescope. Their results suggest that including both systematic and random error, the SSPP has a one-sigma precision of 141 K in  $T_{\text{eff}}$ , 0.23 dex in  $\log g$ , and 0.23 dex in  $[\text{Fe}/\text{H}]$ . The stars bright enough to be observed at high resolution all had  $\text{S/N} \gtrsim 50$  SEGUE spectra, so direct comparison with high-resolution spectra can only be made for high S/N spectra. For that reason, they degraded these high S/N SEGUE spectra with stellar parameters well characterized by high-resolution spectroscopy with a detailed noise model to create many thousand spectra at many values of S/N between 55 and 1. They then ran the SSPP on the noise-degraded spectra to determine the accuracy and precision of the SSPP as a function of S/N and reported the result in Table 6 of Lee et al. (2008a). They found a  $[\text{Fe}/\text{H}]$  precision of (0.5, 0.2, 0.1) dex at S/N of (5, 10, 15) and a  $[\alpha/\text{Fe}]$  precision of 0.1 dex at S/N greater than 20 (Lee et al. 2011). Finally, Lee et al. (2008b) applied the SSPP to stars associated with open and globular clusters, where they

found that the SSPP achieves a precision in [Fe/H] of 0.13 dex over the range  $-0.3 \leq g - r \leq 1.3$ ,  $2.0 \leq \log g \leq 5.0$ , and  $-2.3 \leq [\text{Fe}/\text{H}] \leq 0.0$ .

### 3.2. Coaddition Algorithm

We include in the coadded spectra only those spectra that correspond to MPMSTO stars with radial velocities that indicate membership in the population of interest. In addition, we include in the coadded spectra only those spectra that correspond to MPMSTO stars in a finite range of effective temperature, as the strength of spectral lines is affected by temperature as well as [Fe/H]. Consequently, the  $T_{\text{eff}}$  range has to be small enough to ensure that the coadd gives an accurate [Fe/H] that is representative of the population. In order to estimate the effective temperature of a MPMSTO star from its  $g - r$  color, we fit a linear model between  $g - r$  color and  $T_{\text{eff}}$  in the range  $0.15 < g - r < 0.5$  for all stars in SDSS DR7 with SEGUE spectroscopy at  $\text{S/N} > 40$  and a SSPP  $[\text{Fe}/\text{H}] < -1.0$ . We find that  $T_{\text{eff}} \approx -3800(g - r) + 7300$  with about 500 K of scatter at constant  $g - r$  color. We use  $g - r$  color because the photometric accuracy of the SDSS does not vary over the apparent magnitude range of our MPMSTO sample, while the spectral S/N and therefore  $T_{\text{eff}}$  precision inferred from the spectra varies substantially. Moreover, there are no reliable  $T_{\text{eff}}$  estimates for the half our MPMSTO sample with  $\text{S/N} < 10$ . For those reasons, we use the simple relationship between  $g - r$  color and  $T_{\text{eff}}$  at high S/N to ensure that we reliably include in each coadd spectrum only MPMSTO star spectra in a narrow range of  $T_{\text{eff}}$  even at low S/N. Likewise, the photometric selection and spectroscopic confirmation of MPMSTO stars indicates that the stars in our sample have similar surface gravities. As a result, we ensure that each spectrum that enters into a coadd correspond to a star in a narrow range of  $T_{\text{eff}}$  and  $\log g$ . Therefore, the only unconstrained stellar parameter is metallicity, and a SSPP analysis of the coadded MPMSTO spectrum will produce an unbiased estimate of the mean metallicity of the MPMSTO population.

We shift each MPMSTO spectrum eligible for inclusion in a coadd to a heliocentric radial velocity  $v_r = 0$  km s $^{-1}$ . We then use natural cubic spline interpolation to interpolate both the spectrum and its inverse variance on to a common grid in wavelength. Next, we numerically integrate the area under the curve defined by the spectrum and normalize both the spectrum (by dividing by the normalization factor) and the inverse variance (by multiplying by the normalization factor squared) to ensure that each spectrum that is to be included in the coadd has the same scale. For each population of interest, we then create an ensemble of realizations of the coadded spectrum by bootstrap resampling from the set of radial velocity zeroed, interpolated, and normalized spectra that belong to that population. Each spectrum contributes to each wavelength bin in proportion to its inverse variance in that bin relative to the other spectra selected for coaddition. One danger to this approach is the possibility that the resultant coadded spectrum does not correspond to the spectrum of any physical star. This is unlikely in our analysis though, as we obtain good agreement between globular cluster metallicities produced by coaddition and their known metallicities from high resolution spectroscopy. We describe the coaddition process

in detail in Appendix A.

The SSPP also uses Sloan *ugriz* photometry in its parameter estimation routines, so we determine an equivalent *ugriz* photometric measurement for our coadd spectra by computing a weighted average of the *ugriz* photometric measurement of the individual stars in each bootstrap coadd, using the mean S/N between 3950 Å and 6000 Å as the weight. We then run the SSPP on each of the bootstrap coadded spectra and average *ugriz* photometry to determine the mean of the SSPP [Fe/H] and  $[\alpha/\text{Fe}]$  estimates for that particular MPMSTO population.

### 3.3. Accuracy and Precision in the Ideal Case

To determine the precision and accuracy of our coaddition algorithm as a function of S/N and population metallicity, we analyzed spectra created by coadding individual MPMSTO star spectra that had been observed to very high S/N during the SEGUE survey but that had been subsequently degraded with a detailed noise model. Though this is the ideal case of uniform effective temperature, surface gravity, and metallicity, the result will reveal the amount of bias and variance in our measurements that can be attributed to noise and population metallicity.

Section 6 of Lee et al. (2008a) describes the algorithm used to create the noise degraded spectra we use in this analysis and summarize here. Each SEGUE plate obtains spectra for stars that span a range of magnitudes from  $g \approx 15$  to  $g \approx 20$ , but is exposed to a fiducial S/N for the faint targets. As such, the noise properties of the SEGUE spectra vary with the magnitude and color of the targets, with increasing fractional contribution from the sky for faint targets. Because the observing criteria for the survey were homogeneous, it is possible to parametrize those variations and create a realistic model noise spectrum that can be used to create low S/N realizations of high S/N spectra. Randomly chosen residual spectra from the sky fibers are then added to complete each realization. This noise model was used in Lee et al. (2008b) to test the accuracy of the SSPP, and we use the same model here to test the accuracy of the SSPP parameters of our coadds. We use a sample of 640 noise-added realizations of eight high S/N SEGUE MPMSTO stars with  $[\text{Fe}/\text{H}]$  values from  $-2.41 < [\text{Fe}/\text{H}] < -0.23$ , which spans the metallicity range of our sample. We have 54 realizations at S/N values from 7.5 to 55.

We use this large sample of noise-degraded spectra for eight MPMSTO stars to determine the precision and accuracy of our coaddition algorithm as a function of metallicity and S/N. The analysis of noise-added spectra allows us to examine the performance of the SSPP and our coaddition algorithm over a range of metallicity and S/N that spans our entire sample. We plot the results of our analyses for [Fe/H] in Figure 1 and for  $[\alpha/\text{Fe}]$  in Figure 2. The MSE of our SSPP analysis of coadded spectra created from the coaddition of noise-degraded spectra of single MPMSTO stars ranges from 0.05 dex in both [Fe/H] and  $[\alpha/\text{Fe}]$  for the most iron-rich stars to 0.20 dex in both [Fe/H] and  $[\alpha/\text{Fe}]$  for the most iron-poor stars. In both cases, the range in effective S/N results because the coadded spectra are created by coadding from an ensemble of spectra with different S/N, and the range

of S/N apparent in Figure 1 and Figure 2 is larger than the equivalent range of S/N in the ECHOS. Reassuringly, there is no obvious trend in the precision and accuracy of the bootstrap coaddition process with effective temperature. The outliers at low S/N in Figure 1 and Figure 2 are likely coadded spectra that include very low S/N spectra with large sky residuals, possibly taken from SEGUE plates with below-average sky subtraction. The existence of outliers due to this effect is another reason why the bootstrap resampling from many spectra is important to determine the error distribution that results from the coaddition process. In the next subsection, we will use this analysis of the noise-added data to determine the MSE of our coadditon analysis as function of metallicity and S/N.

#### 3.4. Accuracy and Precision in a Representative Case

In reality, the spectra in each ECHOS coadd correspond to stars in a small but finite range of effective temperature, surface gravity, and composition. In order to determine the degree to which these spreads in properties affects our ability measure the mean metallicity of the ECHOS and smooth halo populations by coadding spectra belonging to each, we analyzed spectra created by coadding individual MPMSTO spectra corresponding to MPMSTO stars that likely belong to the well studied Galactic globular clusters M 13 and M 15. The M 13 and M 15 data are representative of the range in  $T_{\text{eff}}$  and  $\log g$  of a real MPMSTO population as selected by the SEGUE survey. It is exactly the fact that the globular cluster MPMSTO stars occupy a narrow range in [Fe/H] that makes the this globular cluster data so useful—we know the expected [Fe/H] very well and can test whether or not we converge to the known value when coadding from a range of  $T_{\text{eff}}$  and  $\log g$ . Unfortunately, [Fe/H] and  $T_{\text{eff}}$  are degenerate, so we optimize the  $g - r$  range selected in order to produce coadded spectra with the maximum S/N and therefore the most accurate abundance estimate from the SSPP in the following way. Increasing the  $T_{\text{eff}}$  range of spectra that are coadded increases the number of spectra included in each coadd, increases the total signal in each coadd, and ultimately increases the precision of the abundance estimate. The trade off is that coadding spectra in too large a range in  $T_{\text{eff}}$  can decrease the accuracy of the abundance estimate. We find that coadding spectra that belong to stars in 250 K bins produces the same accuracy as the coaddition of stars in 500 K bins, as the scatter in the  $T_{\text{eff}} - g - r$  relation at constant  $g - r$  color is about 500 K. Combined with the fact the coadd spectrum that results from coadding spectra in the 500 K bin always reaches higher S/N (and therefore higher precision) than the coadd spectrum that results from coadding spectra in the 250 K bin, we exclusively use the 500 K bin in our analysis of ECHOS.

We select those stars that have equatorial coordinates that place them within the tidal radius of each cluster (as reported in Harris 1996) and that have radial velocities consistent with cluster membership. Given the precision of SEGUE radial velocities at the S/N of the cluster spectra for cluster members that meet the SEGUE turnoff sample criteria, that corresponds to  $15 \text{ km s}^{-1}$  for M 13 and  $25 \text{ km s}^{-1}$  for M 15. We select for coaddition only those spectra that correspond to MPMSTO stars with  $g - r$  colors that place them within the 500 K bin in effec-

tive temperature that produces the highest S/N coadd. The median S/N of the MPMSTO spectra that remain after applying these cuts is 22.9 from 12 spectra for M 13 and 9.0 from 11 spectra for M 15. The number of spectra in each globular cluster coadd is approximately equivalent to the number of spectra included in each ECHOS coadd.

From the  $n$  MPMSTO spectra that remain after the application of our cuts in equatorial coordinate, radial velocity, and  $g - r$  color, we select with replacement  $m = 1, 2, 3, \dots, n$  spectra from the available data. We coadd the spectra and use the SSPP to derive [Fe/H] and [ $\alpha/\text{Fe}$ ] for that bootstrap coadded spectrum, and save the result. We repeat that process 100 times for each of  $m = 1, 2, 3, \dots, n$  to build up the distribution of SSPP [Fe/H] and [ $\alpha/\text{Fe}$ ] estimates for both globular clusters as a function of S/N. For M 13, the SSPP produces an estimate of  $[\text{Fe}/\text{H}] = -1.7 \pm 0.15$  and  $[\alpha/\text{Fe}] = 0.3 \pm 0.15$ . High-resolution measurements of M 13 by Kraft et al. (1997) and Cohen & Meléndez (2005) yielded  $[\text{Fe}/\text{H}] = -1.59$  with  $[\alpha/\text{Fe}] = 0.22$  and  $[\text{Fe}/\text{H}] = -1.55$  with  $[\alpha/\text{Fe}] = 0.26$  respectively. Likewise, for M 15 we find that  $[\text{Fe}/\text{H}] = -2.4 \pm 0.2$  and  $[\alpha/\text{Fe}] = 0.3 \pm 0.2$ . High-resolution measurements of M 15 by Sneden et al. (1997) and Sneden et al. (2000b) yielded  $[\text{Fe}/\text{H}] = -2.19$  with  $[\alpha/\text{Fe}] = 0.38$  and  $[\text{Fe}/\text{H}] = -2.28$  with  $[\alpha/\text{Fe}] = 0.40$  respectively. We present the results for M 13 in Figure 3 and the results for M 15 in Figure 4. This implies that at the resolution of the SEGUE spectra and for the range of  $T_{\text{eff}}$  and  $\log g$  included in the coadds, S/N is the dominant contribution to the MSE in estimating the average metallicity of a population using the ensemble of bootstrap coadds. At the same time, these results compare favorably to those presented in Lee et al. (2008a,b) and Allende Prieto et al. (2008), as we measure the performance of the SSPP on a subset of the SEGUE data in a narrow range in  $g - r$  color.

We summarize the precision and accuracy of our SSPP analysis of coadded spectra in Figure 5. The precision and accuracy of our SSPP analysis is a function of metallicity; consequently, our estimates are most precise and accurate ( $\sim 0.1$  dex in [Fe/H] and [ $\alpha/\text{Fe}$ ]) for the most metal-rich populations, and least precise and accurate for the most metal-poor populations ( $\sim 0.2$  dex in [Fe/H] and [ $\alpha/\text{Fe}$ ]). Moreover, we find that at equivalent metallicity, the MSE we compute for M 13 and M 15 based on coadd spectra created by coadding MPMSTO spectra in a finite range of effective temperature and surface gravity are in good agreement with the MSE computed in the ideal case of constant effective temperature and surface gravity for coadds based on noise-degraded MPMSTO spectra. As a result, we use the precision we derived for the SSPP metallicity analysis of the noise-added spectra to characterize the precision of our ECHOS metallicity measurements. For that reason, including both statistical and systematic effects, our SSPP analysis of coadded SEGUE MPMSTO spectra produces estimates that are sufficiently precise and accurate to identify chemical differences between ECHOS and the kinematically smooth inner halo MPMSTO population on the order  $\sim 0.2$  dex in both [Fe/H] and [ $\alpha/\text{Fe}$ ]. We use the expected MSE as a function of metallicity and S/N given in Figure 5 to determine whether an ECHOS is chemically distinct from the kinematically smooth halo MPMSTO popula-

tion along the same line of sight.

### 3.5. The Metallicity of ECHOS

For each of the three classes of ECHOS from S09, we consider for coaddition those spectra that correspond to stars within a radial velocity overdensity and therefore consistent with ECHOS membership. As defined in S09, a radial velocity overdensity is a group of MPMSTO stars observed with radial velocities within a narrow range such that the group is extraordinarily unlikely to be observed if the underlying population were kinematically smooth. For the bin detections, we coadd the spectra of stars in the  $20 \text{ km s}^{-1}$  bin that contains the significant detection. For the peak detections, we coadd the spectra of stars within the measured width of the peak in the cumulative distribution function (the  $\Theta$  statistic of S09). The width of the peak in  $\Theta$  is the same as the velocity dispersion quoted for each ECHOS in Tables 2 and 3.

As before, we select those stars within the  $500 \text{ K}$  wide bin in effective temperature that produces the highest S/N in the resultant coadded spectrum. We shift each candidate spectrum to  $v_r = 0 \text{ km s}^{-1}$  and interpolate the spectrum and its inverse variance on to a common wavelength grid, and rescale each spectrum and its inverse variance to a common scale. From the  $n$  radial velocity selected, temperature controlled, radial velocity zeroed, interpolated, and scaled MPMSTO spectra, we sample  $n$  with replacement and coadd the spectra to create a single bootstrap realization of the resultant coadded spectrum distribution. For each ECHOS, we repeat the resampling process 100 times to create 100 bootstrap coadded spectra. We then run the SSPP on all of the bootstrap coadded spectra to determine the distribution of measured  $[\text{Fe}/\text{H}]$  and  $[\alpha/\text{Fe}]$  for the ensemble of realizations.

As a control, along the same line of sight as each ECHOS we perform the same steps on all the MPMSTO spectra that are associated with the kinematically smooth halo population. As a result, the stars in the control sample are in the same volume, were observed at the same time, and have a similar range of magnitude and S/N as the stars in the ECHOS. In that way, we can characterize the mean of  $[\text{Fe}/\text{H}]$  and  $[\alpha/\text{Fe}]$  and estimate the error in our estimate of the mean for both the ECHOS and the kinematically smooth population along the same line of sight. With that information, any observed difference in composition is unlikely to result from systematic effects. Consequently, any observed chemical offset between an ECHOS and the kinematically smooth inner halo MPMSTO population along the same line of sight likely results from genuine chemical differences.

We report the results of these calculations for all of the ECHOS discovered in S09 in Figure 6 through Figure 11 and in tabular form in Table 1 through Table 3. In Figure 6 through Figure 11, the precision of our SSPP analysis is best characterized by the scatter apparent in results of the bootstrap coaddition process for both ECHOS and the kinematically smooth halo. If the two clouds of points do not overlap, than the two populations are chemically distinct. We quantify this scatter and report the result in Table 1 through Table 3. In all cases where the quoted metallicity of the smooth component is more iron-rich than typically associated with the smooth inner halo, the reason is because the ECHOS dominates the MPMSTO population along that line of

sight (see Figures 2 through 11 of S09). As a result, it is difficult to identify a large enough sample of stars in the kinematically smooth inner halo MPMSTO population for the equivalent analysis, so the quoted metallicity of the smooth halo can be significantly influenced by the metallicity of the ECHOS.

## 4. DISCUSSION

### 4.1. The Kinematic and Chemical Properties of ECHOS

We searched for correlations between the dynamical properties of ECHOS from S09 and the chemical properties determined in this analysis. For the rest of this section, we examine the properties of the 21 Class II peak ECHOS from Table 3 of S09. That sample of 21 ECHOS is both the largest sample and the most representative sample of the inner halo ECHOS population. In general, we find that ECHOS that are iron-rich also have large radial velocity dispersions and are the most prominent ECHOS in that they have high number densities and are fractionally the largest contributors to the MPMSTO population along the line of sight where they were discovered; we plot these relations in Figure 12. Though large velocity dispersions are found only for the most metal-rich ECHOS, small velocity dispersions are found at all metallicities. The prominence of metal-rich substructures was predicted by Font et al. (2006), as metal-rich substructures are preferentially produced by the most luminous progenitors. We find no significant correlation between  $[\text{Fe}/\text{H}]$  or  $[\alpha/\text{Fe}]$  and distance.

We initially identified ECHOS because they are kinematically distinct from the kinematically smooth inner halo MPMSTO population. As we showed in Figure 6 through Figure 11, nearly all ECHOS are also chemically distinct from the background smooth inner halo MPMSTO population along the same line of sight. We summarize this chemical distinctiveness in Figure 13. As a population, ECHOS are more iron-rich but less  $\alpha$ -enhanced than the kinematically smooth background inner halo MPMSTO population. We showed in S09 that 10% of the inner halo (by volume) has 30% of its MPMSTO population in ECHOS. Combined with the observation that ECHOS are metal-rich, these facts suggest that the most likely metallicity for an accreted star in the inner halo is  $[\text{Fe}/\text{H}] \sim -1$ . At ECHOS  $[\text{Fe}/\text{H}] \gtrsim -1$ , the apparent correlation between the iron metallicity of ECHOS and the iron metallicity of the smooth component of the halo results from the fact that iron-rich ECHOS are also the most prominent ECHOS (see Figure 12). That is, since the iron-rich ECHOS make up such a large fraction of the halo MPMSTO population along the line of sight where they were discovered, it is difficult to isolate a sample of MPMSTO stars in the kinematically smooth halo population.

To asses the statistical significance of the observation that the population of ECHOS is more iron-rich but less  $\alpha$ -enhanced than the kinematically smooth background inner halo MPMSTO population, we used a Monte Carlo simulation. Imagine that ECHOS and the kinematically smooth component of the halo really did have the same chemical composition. In that case, in Figure 13 the departure of the points from the line  $y = x$  must result from imperfect observation, characterized by the error bars in the plot. Under that null hypothesis, we sam-

ple each ECHOS composition from a normal distribution centered on the line  $y = x$  with standard deviation equal to the error in our measurement of the composition of the ECHOS. Likewise, we sample the composition of the smooth component along each line of sight from a normal distribution centered on the same point on the line  $y = x$  with standard deviation equal to the error in our measurement of the composition of the smooth component. We compute the signed, cumulative Euclidean distance of the entire population from the line  $y = x$ , and save the result. We repeat this process  $10^6$  times. We find that under the null hypothesis, in no instance does the Monte Carlo simulation produce a cumulative distance of each point from the line  $y = x$  equal to the cumulative distance observed in the ECHOS [Fe/H] distribution. Therefore the probability that the population of ECHOS has the same [Fe/H] as the smooth population along each line of sight in which we discovered an ECHOS is less than  $10^{-6}$ . Our  $[\alpha/\text{Fe}]$  estimates are much less precise than our [Fe/H] estimates; nevertheless, the probability that the population of ECHOS has the same  $[\alpha/\text{Fe}]$  as the smooth population along each line of sight in which we discovered an ECHOS is about  $10^{-3}$ . The fact that ECHOS, as a population, are so chemically distinct from the smooth background inner halo MPMSTO population along the same line of sight strongly supports the kinematic substructure identifications in S09.

The stars in ECHOS preferentially have apparent magnitudes that place them in the most distant half of our MPMSTO sample (Schlaufman et al. 2009). As a result, it is possible that the chemical distinctiveness of ECHOS is the result of a metallicity gradient in the inner halo. To test this hypothesis, we considered only those lines of sight that were not targeted at a known element of substructure and for which we had no significant ECHOS detection of any kind. In other words, those lines of sight which are dominated by the smooth component of the halo. For every MPMSTO star in that sample, we very roughly estimate the distance to each star according to the procedure described in Section 2 of S09. We then split the sample in half at about 14 kpc: the nearest 50% of the MPMSTO population goes into the “close” subsample and the farthest 50% of the MPMSTO population goes into the “far” subsample.

Then, for each subsample, we compute line of sight average metallicities by the same spectral coaddition process described in Section 3. In that way, we end up with two estimates for the average chemical composition of MPMSTO stars in the smooth component along each line of sight where there is no significant substructure – an estimate for the “close” subsample and estimate for the “far” subsample. We find that the average metallicity for the “close” subsample is  $[\text{Fe}/\text{H}] = -1.7 \pm 0.1$  while the average metallicity for the “far” subsample is  $[\text{Fe}/\text{H}] = -1.5 \pm 0.1$ . Meanwhile, the average metallicity of our ECHOS is  $[\text{Fe}/\text{H}] = -1.1 \pm 0.1$ . For that reason, the apparent chemical distinctiveness of ECHOS is unlikely to be the result of a metallicity gradient in the inner halo. Indeed, though the halo is potentially chemically inhomogeneous on large scales (e.g., Carollo et al. 2007, 2010), our analysis is confined to a relatively small region in the inner halo.

ECHOS are also chemically distinct from the other

components of the Milky Way. The average level of star formation appears to have been more or less continuous in the thin disk for many Gyr (Rocha-Pinto et al. 2000a,b), so thermonuclear SN have had plenty of time to contribute to the chemistry of the ISM. Consequently stars in the thin disk are typically close to solar in both  $[\text{Fe}/\text{H}]$  and  $[\alpha/\text{Fe}]$ . The origin of thick disk stars is unclear, though they are uniformly more  $\alpha$ -enhanced than thin-disk stars at constant  $[\text{Fe}/\text{H}]$  (e.g., Bensby et al. 2005; Reddy et al. 2006; Bensby et al. 2007). In Figure 14 we plot our ECHOS in the  $[\text{Fe}/\text{H}]-[\alpha/\text{Fe}]$  plane along with  $[\text{Fe}/\text{H}]$  and  $[\alpha/\text{Fe}]$  estimates for individual stars from Edvardsson et al. (1993), Nissen & Schuster (1997), Hanson et al. (1998), Fulbright (2000), Prochaska et al. (2000), Stephens & Boesgaard (2002), Bensby et al. (2003), and Reddy et al. (2003) and presented in Venn et al. (2004). We plot only those stars from Venn et al. (2004) that have a better than 50% association probability with the thin disk, thick disk, or halo as indicated by their  $U$ ,  $V$ , and  $W$  velocities. ECHOS are found in a region of the  $[\text{Fe}/\text{H}]-[\alpha/\text{Fe}]$  plane sparsely populated—but not completely devoid of—individual stars. In general, ECHOS are: (1) more iron-rich and less  $\alpha$ -enhanced than halo stars, (2) more iron-poor than typical thick-disk stars, and (3) more iron-poor and more  $\alpha$ -enhanced than typical thin-disk stars. As a result, most stars associated with recent accretion events are more metal-rich than the average metallicity of the inner halo. In Figure 15, we plot the location of ECHOS in the  $[\text{Fe}/\text{H}]-[\alpha/\text{Fe}]$  plane along with the location of individual giant stars in eight dSph galaxies reported in Kirby et al. (2010). If ECHOS are the debris of a tidally disrupted dSph, Figure 15 indicates that the progenitor may have been comparable to the Sculptor or Leo I dSph galaxies.

Interestingly, there may be a hint in the Venn et al. (2004) compilation that those stars that are on retrograde orbits are the halo stars with  $[\alpha/\text{Fe}]$  most like the stars in the ECHOS (though the ECHOS have higher iron metallicity). Several studies using nearby halo star samples have found correlations between increased scatter or peculiar elemental abundance patterns and extreme kinematics (Carney et al. 1997; Fulbright 2002; Ivans et al. 2003; Roederer 2009; Carollo et al. 2007, 2010). These studies find that metal-poor stars belonging to the distant, outer halo originated in a more varied and/or inhomogeneous environment, in support of the idea that the outer halo is assembled by more recent accretion of many low-mass systems. However, those studies are limited to  $[\text{Fe}/\text{H}] < -1$ , and our results demonstrate that for stars currently in the inner halo region of the Galaxy, most stars accreted in the last 5 Gyr are not metal-poor, but instead have  $[\text{Fe}/\text{H}] \sim -1$ . Any comprehensive study of the halo accretion history must include stars over a broad range in metallicity. A direct comparison between our results and the metal-poor samples would require an analysis of selection biases in those samples that is beyond the scope of this paper (for a discussion of the issues see Roederer 2009), but we note that the sample of halo stars in which the ECHOS were identified was selected using ultraviolet excess, which would tend to bias our sample against metal-rich stars (see S09 for details).

In Figure 16 we compare the velocity dispersions of ECHOS from S09 with the median radial velocity pre-

cision of the MPMSTO stars in each ECHOS. In this case, the radial velocity precision as a function of S/N we used in S09 assumed a population metallicity of  $[\text{Fe}/\text{H}] \sim -1.6$ . SEGUE radial velocity precision becomes better at higher metallicities, so the fact that ECHOS have  $[\text{Fe}/\text{H}] \sim -1.0$  may indicate the actual radial velocity precision is somewhat better. In any case, we find many of our ECHOS have velocity dispersions that are substantially larger than the expected radial velocity precision.

#### 4.2. The Origin of ECHOS

The stars in ECHOS are more iron-rich and less  $\alpha$ -enhanced than the typical inner halo MPMSTO star population. They are also more iron-poor than typical thick-disk stars but more  $\alpha$ -enhanced than typical thin-disk stars. The high  $[\text{Fe}/\text{H}]$  metallicity of ECHOS almost certainly rules out ultrafaint dSph galaxies as ECHOS progenitors, as ultrafaint dSph galaxies have average  $[\text{Fe}/\text{H}] \lesssim -2$  (e.g., Kirby et al. 2008b). If ECHOS are the tidal debris of one or more dSph galaxies, the dSph luminosity–metallicity relation (e.g., Kirby et al. 2008b) implies a progenitor luminosity of  $L \sim 10^8 L_\odot$  to produce a characteristic iron metallicity  $[\text{Fe}/\text{H}] \sim -1.0$ . That luminosity combined with a reasonable dSph stellar mass to light ratio  $M_*/L_V \sim 3$  and total mass to light ratio  $M_{\text{tot}}/L_V \sim 10$  (e.g., Mateo 1998) implies the accretion of a progenitor with stellar mass  $M_* \sim 3 \times 10^8 M_\odot$  and total mass  $M_{\text{tot}} \sim 10^9 M_\odot$ , comparable to Local Group members NGC 147 or NGC 185. Radial velocity substructures persist for many crossing times, and because the typical crossing time in the inner halo is 50 Myr ECHOS should be observable for up to 5 Gyr (see Section 5.1 of S09). As a result, if the debris of an ECHOS progenitor is still visible as cold radial velocity substructure, the accretion event must have occurred in the last  $\sim 5$  Gyr, or equivalently, since  $z = 0.5$ . Such accretion events are common in the accretion histories of Milky Way analog halos, and a typical halo might have experienced 10 such accretion events since  $z = 0.5$  (e.g., Stewart et al. 2008; Fakhouri et al. 2010). Again, the distribution of ECHOS in the  $[\text{Fe}/\text{H}]-[\alpha/\text{Fe}]$  plane is similar to the distribution in  $[\text{Fe}/\text{H}]-[\alpha/\text{Fe}]$  plane of individual giant stars in the Sculptor dSph (Kirby et al. 2010).

The radial velocity dispersion distribution of ECHOS may also be a clue to their origin. Collisionless dynamics implies that as the position space component of the phase-space distribution of a tidally disrupted stellar system becomes hotter, the velocity component of its phase-space distribution must necessarily become colder (e.g., Binney & Tremaine 1987). In other words, as a tidally disrupted stellar system spreads across the sky its velocity dispersion measured over a small patch of sky must decrease with time. For that reason, the radial velocity dispersion of an element of cold halo substructure is a lower limit on the radial velocity dispersion of its progenitor. At the same time, multiple wraps of stream-like substructure might give the appearance of a single substructure with large velocity dispersion, though there is both observational evidence (e.g., Bell et al. 2008) and theoretical modeling (Johnston et al. 2008) that suggests stream-like substructures are rare in inner halo. If ECHOS really are shell-like substructures on radial orbits as opposed to stream-like substructures on tangential or-

bits as proposed by S09, measurement over a small patch of sky might still intersect orbits in a range of orbital phase and therefore produce large velocity dispersions that are not representative of the velocity dispersion of the progenitor. We argue that this is unlikely, however, as that would imply that the radial velocity dispersion within a single ECHOS is a function of apparent magnitude, a trend not observed in ECHOS (see Figures 2 through 11 in S09). With those caveats in mind, typical classical dwarf spheroidal (dSph) galaxies have radial velocity dispersions  $\sigma \sim 10 \text{ km s}^{-1}$  (e.g., Mateo 1998). Indeed, three of our ECHOS even have velocity dispersions comparable to that observed in the Small Magellanic Cloud (SMC) in which Harris & Zaritsky (2006) measured  $\sigma \approx 27.5 \pm 0.5 \text{ km s}^{-1}$ . The median radial velocity dispersion of ECHOS  $\sigma \sim 20 \text{ km s}^{-1}$  is also characteristic of a dSph like NGC 147 or NGC 185. This observation implies an even more massive progenitor though, as the fact that ECHOS are not associated with surface brightness substructure suggests that the velocity dispersion has had time to cool measurably.

The observation that ECHOS are less  $\alpha$ -enhanced than typical inner halo stars suggests that the star formation timescale in the ECHOS progenitor was long relative to the star formation timescale in the massive progenitor of the bulk of the inner halo (e.g., McWilliam et al. 1995), so long as the stellar initial mass function is not too different in the two environments. This relatively extended star formation timescale might disfavor globular clusters as ECHOS progenitors, though some globular clusters have  $[\alpha/\text{Fe}] \sim 0.2$  (e.g., Carney 1996; Brodie & Strader 2006; Carretta et al. 2009). On the other hand, the characteristic ECHOS  $[\text{Fe}/\text{H}] \sim -1.0$  falls between the two peaks in the observed bimodal Milky Way globular cluster  $[\text{Fe}/\text{H}]$  distribution (e.g., Armandroff & Zinn 1988; Brodie & Strader 2006). Additionally, globular clusters that are metal-rich are very rare in the inner halo (e.g., Geisler et al. 2007). In any case, the large radial velocity dispersion of ECHOS indicates that ECHOS are unlikely to be the debris of tidally disrupted globular clusters, as globular clusters have velocity dispersions  $\sigma \sim 5 \text{ km s}^{-1}$  (e.g., Mandushev et al. 1991). Core-collapse globular clusters have higher velocity dispersions, but are also resistant to disruption.

One last possibility is that the stars in ECHOS formed in the nascent disk of the Milky Way and were scattered into the inner halo during an accretion event. Recent cosmological models of Milky Way formation by Zolotov et al. (2009) suggest that scattering into the inner halo does contribute to the stellar population in the inner halo. Moreover, the accretion of dSph galaxies more massive than those suggested by the characteristic ECHOS  $[\text{Fe}/\text{H}] \sim -1.0$  can scatter substantial numbers of disk stars into the inner halo (e.g., Purcell et al. 2010). However, models of the chemical evolution of the disk of the Milky Way suggest that the typical chemical composition of ECHOS is difficult to explain with a disk population (Schönrich & Binney 2009a,b). In addition, Zolotov et al. (2010) recently suggested that disk stars scattered into the halo should be more  $\alpha$ -enhanced than inner halo stars at constant  $[\text{Fe}/\text{H}]$ . Improved resolution and better treatments of star formation and feedback in theoretical models may yet determine whether scattering

of disk stars into the inner halo by low-mass accretion events is a plausible origin of ECHOS.

## 5. CONCLUSION

The metal-poor main sequence turnoff stars in the elements of cold halo substructure in the inner halo of the Milky Way found to be kinematically distinct from the kinematically smooth inner halo population by Schlaufman et al. (2009) are also chemically distinct from the smooth inner halo. As a population, ECHOS are more iron-rich and less  $\alpha$ -enhanced than the MPM-STO stars in the kinematically smooth halo population along the same line of sight. ECHOS are chemically distinct from both the thin and thick disk as well, as they are more iron-poor than average thick-disk stars and both more iron-poor and more  $\alpha$ -enhanced than average thin-disk stars. Kinematically, the typical velocity dispersion of the ECHOS population is  $\sigma \sim 20 \text{ km s}^{-1}$ , though ECHOS have a range of radial velocity dispersions extending from the floor of  $\sigma \sim 10 \text{ km s}^{-1}$  set by the precision of SEGUE radial velocities at the apparent magnitude of the stars in ECHOS to the maximum observed value of  $\sigma \sim 30 \text{ km s}^{-1}$ . If ECHOS are the result of the tidal disruption of an accreted dwarf spheroidal galaxy or galaxies, the high iron metallicity  $[\text{Fe}/\text{H}] \sim -1.0$ , large velocity dispersion  $\sigma \sim 20 \text{ km s}^{-1}$ , and the lack of corresponding surface brightness substructure imply the accretion of a  $M_{\text{tot}} \gtrsim 10^9 M_{\odot}$  halo sometime in the last 5 Gyr since  $z = 0.5$ . In addition, the high iron metallicities, low  $\alpha$ -enhancements, and large velocity dispersions are difficult to reconcile with globular clusters as the progenitors of ECHOS. One final possible explanation for these observations is that the stars in ECHOS formed in the nascent disk of the Milky Way and were subsequently scattered into the inner halo by cosmologically common low-mass accretion events, though models of the chemical evolution of the Milky Way's disk cast some doubt on this scenario as well.

We thank James Bullock, Puragra Guhathakurta, Evan Kirby, Piero Madau, Sarah Martell, Ralph Schönrich, and Matthias Steinmetz for useful comments and conversation. We also thank the anonymous referee for suggestions that improved the clarity of this manuscript. This research has made use of NASA's Astrophysics Data System Bibliographic Services. This material is based upon work supported under a National Science Foundation Graduate Research Fellowship. Y.S.L. and T.C.B. acknowledge partial support for this work from PHY 02-16783 and PHY 08-22648: Physics Frontiers Center / Joint Institute for Nuclear Astrophysics (JINA), awarded by the U.S. National Science Foundation. Funding for the SDSS and SDSS-II has been provided by the Alfred P. Sloan Foundation, the Participating Institutions, the National Science Foundation, the U.S. Department of Energy, the National Aeronautics and Space Administration, the Japanese Monbukagakusho, the Max Planck Society, and the Higher Education Funding Council for England. The SDSS Web Site is <http://www.sdss.org/>.

The SDSS is managed by the Astrophysical Research Consortium for the Participating Institutions. The Participating Institutions are the American Museum of Natural History, Astrophysical Institute Potsdam, University of Basel, University of Cambridge, Case Western Reserve University, University of Chicago, Drexel University, Fermilab, the Institute for Advanced Study, the Japan Participation Group, Johns Hopkins University, the Joint Institute for Nuclear Astrophysics, the Kavli Institute for Particle Astrophysics and Cosmology, the Korean Scientist Group, the Chinese Academy of Sciences (LAMOST), Los Alamos National Laboratory, the Max-Planck-Institute for Astronomy (MPIA), the Max-Planck-Institute for Astrophysics (MPA), New Mexico State University, Ohio State University, University of Pittsburgh, University of Portsmouth, Princeton University, the United States Naval Observatory, and the University of Washington.

*Facilities:* Sloan

## APPENDIX

### A. DETAILED DESCRIPTION OF COADDITION ALGORITHM

The selection of the input sample of spectra to the coaddition process is different in each of the three contexts described in Sections 3.3, 3.4, and 3.5. In all cases, we select a bootstrap sample of spectra, coadd the spectra in the bootstrap sample into a single coadded spectrum, and then use the SSPP to analyze the coadded spectrum. That analysis produces a single estimate of the mean metallicity of the population of stars from which the bootstrap sample was drawn. We draw many bootstrap samples, derive many estimates of the mean metallicity of the population, and use that distribution to quantify both the mean metallicity of the population and our uncertainty in that estimate.

In Section 3.3, we estimate the accuracy and precision of the SSPP on coadded spectra in a range of metallicity ( $-2.41 < [\text{Fe}/\text{H}] < -0.23$ ) and S/N ( $10 \lesssim \text{S/N} \lesssim 100$ ). For each of eight MPMSTO stars with metallicity known from high resolution spectroscopy, the input sample is a collection of 640 spectra produced by adding noise to the original high S/N SEGUE spectrum of that star. There are no radial velocity or effective temperature cuts applied in this case.

In Section 3.4, we estimate the accuracy and precision of the SSPP on coadded spectra produced by bootstrap sampling from the MPMSTO populations of the globular clusters M 13 and M 15. In this case, though the individual spectra belong to stars with very similar metallicities, the spectra will correspond to stars with different radial velocities and effective temperature. As a result, we can use the spectra associated with M 13 and M 15 MPMSTO stars to quantify the effect of coadding stars in a finite range of effective temperature, surface gravity, and radial velocity. Specifically, we include in the sample of input spectra only those spectra corresponding to MPMSTO stars with equatorial coordinates within the projected tidal radius of each cluster, with radial velocities close to the systematic radial velocity of the cluster, and within the 500 K range of effective temperature that produces the highest S/N in the final coadded spectrum.

In Section 3.5, we use our algorithm to estimate both the average metallicity of MPMSTO stars in ECHOS and in the kinematically smooth component of the halo along the same line of sight. We include in each ECHOS sample of input spectra only those spectra corresponding to MPMSTO stars with radial velocities within the radial velocity overdensity that defines the ECHOS (as defined in S09 and reported in Tables 1, 2, and 3). We include all other MPMSTO spectra obtained along the line of sight in the kinematically smooth halo input sample. In both cases, we use the same effective temperature criteria used in the globular cluster case.

The following eight steps describe how a single bootstrap coadded spectrum can be produced from the input samples described above.

1. Use resampling with replacement to select  $N$  spectra from the  $N$  available spectra to create a bootstrap sample of spectra to synthesize into a single coadd spectrum.
2. Let  $f_{i,j}(\lambda'_j)$  and  $g_{i,j}(\lambda'_j)$  denote the flux and inverse variance from the SDSS spectroscopic reduction pipeline. The subscript  $i$  refers to the  $i$ th star in the coadd and the subscript  $j$  refers to the  $j$ th wavelength bin.
3. Shift each spectrum to redshift  $z = 0$  such that

$$\lambda_j = \frac{\lambda'_j}{1+z} \quad (\text{A1})$$

and denote the radial-velocity zeroed spectrum and inverse variance  $f_{i,j}(\lambda_j)$  and  $g_{i,j}(\lambda_j)$  respectively.

4. Use natural cubic spline interpolation to interpolate  $f_{i,j}(\lambda_j) \rightarrow f_i(\lambda)$  and  $g_{i,j}(\lambda_j) \rightarrow g_i(\lambda)$ .
5. Sample the continuous functions  $f_i(\lambda)$  and  $g_i(\lambda)$  on to a common grid in  $\lambda_k$  for every star from  $\lambda_1 = 3850 \text{ \AA}$  to  $\lambda_2 = 9000 \text{ \AA}$  in  $n$  0.5  $\text{\AA}$  increments. Set any  $f_{i,k}(\lambda_k) < 0$  to  $f_{i,k}(\lambda_k) = 0$  and any  $g_{i,k}(\lambda_k) \leq 0$  to  $g_{i,k}(\lambda_k) = 10^{-6}$ .
6. To this point, each star has a different total flux in its spectrum, so rescale  $f_i$  and  $g_i$  to the same total flux while conserving the S/N ratio in each bin. In other words,

$$A_i = \int_{\lambda_1}^{\lambda_2} f_i(\lambda) d\lambda \quad (\text{A2})$$

$$f_{i,k}(\lambda_k) = \frac{1}{A_i} f_i(\lambda_k) \quad (\text{A3})$$

$$g_{i,k}(\lambda_k) = A_i^2 g_i(\lambda_k). \quad (\text{A4})$$

7. Loop over all  $n$  wavelength bins to create the coadd spectrum and its inverse variance using the weighted-mean such that

$$w_i = \{g_{1,k}(\lambda_k), g_{2,k}(\lambda_k), \dots, g_{N,k}(\lambda_k)\} \quad (\text{A5})$$

$$\bar{f}_k(\lambda_k) = \frac{\sum_{i=1}^N w_i f_{i,k}(\lambda_k)}{\sum_{i=1}^N w_i} \quad (\text{A6})$$

$$\bar{g}_k(\lambda_k) = \sum_{i=1}^N w_i. \quad (\text{A7})$$

8. The coadded spectrum  $\bar{f}_k(\lambda_k)$  and its inverse variance  $\bar{g}_k(\lambda_k)$  are then processed by the SSPP to produce a single estimate of the mean metallicity of the input sample.

A single iteration of these eight steps produces a single estimate of the mean metallicity of the input sample, corresponding to a single point in Figures 1 through 4 and Figures 6 through 11. We repeat these eight steps many times to produce many estimates of the mean metallicity of the input sample. We use that distribution to estimate both the true mean metallicity of the input sample and our uncertainty in that estimate.

## REFERENCES

- Abazajian, K. N., et al. 2009, ApJS, 182, 543  
 Allende Prieto, C., Beers, T. C., Wilhelm, R., Newberg, H. J., Rockosi, C. M., Yanny, B., & Lee, Y. S. 2006, ApJ, 636, 804  
 Allende Prieto, C., et al. 2008, AJ, 136, 2070  
 An, D., et al. 2009, ApJ, 707, L64

- Armandroff, T. E., & Zinn, R. 1988, AJ, 96, 92
- Bastian, N., Covey, K. R., & Meyer, M. R. 2010, ARA&A, 48, 339
- Bell, E. F., et al. 2008, ApJ, 680, 295
- Belokurov, V., Evans, N. W., Irwin, M. J., Hewett, P. C., & Wilkinson, M. I. 2006, ApJ, 637, L29
- Belokurov, V., et al. 2007, ApJ, 658, 337
- Bensby, T., Feltzing, S., & Lundström, I. 2003, A&A, 410, 527
- Bensby, T., Feltzing, S., Lundström, I., & Ilyin, I. 2005, A&A, 433, 185
- Bensby, T., Zenn, A. R., Oey, M. S., & Feltzing, S. 2007, ApJ, 663, L13
- Binney, J., & Tremaine, S. 1987, Galactic Dynamics (Princeton, NJ: Princeton Univ. Press)
- Brodie, J. P., & Strader, J. 2006, ARA&A, 44, 193
- Carney, B. W. 1996, PASP, 108, 900
- Carney, B. W., Wright, J. S., Sneden, C., Laird, J. B., Aguilar, L. A., & Latham, D. W. 1997, AJ, 114, 363
- Carollo, D., et al. 2007, Nature, 450, 1020
- Carollo, D., et al. 2010, ApJ, 712, 692
- Carretta, E., Bragaglia, A., Gratton, R., & Lucatello, S. 2009, A&A, 505, 139
- Chiba, M., & Yoshii, Y. 1998, AJ, 115, 168
- Chiba, M., & Beers, T. C. 2000, AJ, 119, 2843
- Cohen, J. G., & Meléndez, J. 2005, AJ, 129, 303
- Duffau, S., Zinn, R., Vivas, A. K., Carraro, G., Méndez, R. A., Winnick, R., & Gallart, C. 2006, ApJ, 636, L97
- Edvardsson, B., Andersen, J., Gustafsson, B., Lambert, D. L., Nissen, P. E., & Tomkin, J. 1993, A&A, 275, 101
- Fakhouri, O., Ma, C.-P., & Boylan-Kolchin, M. 2010, MNRAS, 857
- Freeman, K., & Bland-Hawthorn, J. 2002, ARA&A, 40, 487
- Font, A. S., Johnston, K. V., Bullock, J. S., & Robertson, B. E. 2006, ApJ, 646, 886
- Fukugita, M., Ichikawa, T., Gunn, J. E., Doi, M., Shimasaku, K., & Schneider, D. P. 1996, AJ, 111, 1748
- Fulbright, J. P. 2000, AJ, 120, 1841
- Fulbright, J. P. 2002, AJ, 123, 404
- Geisler, D., Wallerstein, G., Smith, V. V., & Casetti-Dinescu, D. I. 2007, PASP, 119, 939
- Gilmore, G., Wyse, R. F. G., & Norris, J. E. 2002, ApJ, 574, L39
- Gómez, F. A., & Helmi, A. 2010, MNRAS, 401, 2285
- Grillmair, C. J., & Johnson, R. 2006, ApJ, 639, L17
- Grillmair, C. J., & Dionatos, O. 2006, ApJ, 643, L17
- Grillmair, C. J. 2009, ApJ, 693, 1118
- Gunn, J. E., et al. 1998, AJ, 116, 3040
- Gunn, J. E., et al. 2006, AJ, 131, 2332
- Hanson, R. B., Sneden, C., Kraft, R. P., & Fulbright, J. 1998, AJ, 116, 1286
- Harris, W. E. 1996, AJ, 112, 1487
- Harris, J., & Zaritsky, D. 2006, AJ, 131, 2514
- Helmi, A., White, S. D. M., de Zeeuw, P. T., & Zhao, H. 1999, Nature, 402, 53
- Helmi, A., Navarro, J. F., Nordström, B., Holmberg, J., Abadi, M. G., & Steinmetz, M. 2006a, MNRAS, 365, 1309
- Helmi, A., et al. 2006b, ApJ, 651, L121
- Helmi, A. 2008, A&A Rev., 15, 145
- Hogg, D. W., Finkbeiner, D. P., Schlegel, D. J., & Gunn, J. E. 2001, AJ, 122, 2129
- Ivans, I. I., Sneden, C., James, C. R., Preston, G. W., Fulbright, J. P., Höflich, P. A., Carney, B. W., & Wheeler, J. C. 2003, ApJ, 592, 906
- Ivezić, Ž., et al. 2000, AJ, 120, 963
- Ivezić, Ž., et al. 2004, Astronomische Nachrichten, 325, 583
- Ivezić, Ž., et al. 2008, ApJ, 684, 287
- Johnston, K. V., Bullock, J. S., Sharma, S., Font, A., Robertson, B. E., & Leitner, S. N. 2008, ApJ, 689, 936
- Jurić, M., et al. 2008, ApJ, 673, 864
- Kepley, A. A., et al. 2007, AJ, 134, 1579
- Kirby, E. N., Guhathakurta, P., & Sneden, C. 2008a, ApJ, 682, 1217
- Kirby, E. N., Simon, J. D., Geha, M., Guhathakurta, P., & Frebel, A. 2008b, ApJ, 685, L43
- Kirby, E. N., et al. 2010, ApJS, 191, 352
- Klement, R., Fuchs, B., & Rix, H.-W. 2008, ApJ, 685, 261
- Klement, R., et al. 2009, ApJ, 698, 865
- Kraft, R. P., Sneden, C., Smith, G. H., Shetrone, M. D., Langer, G. E., & Pilachowski, C. A. 1997, AJ, 113, 279
- Lee, Y. S., et al. 2008a, AJ, 136, 2022
- Lee, Y. S., et al. 2008b, AJ, 136, 2050
- Lee, Y. S., et al. 2011, AJ, 141, 90
- Majewski, S. R., Munn, J. A., & Hawley, S. L. 1996, ApJ, 459, L73
- Majewski, S. R., Skrutskie, M. F., Weinberg, M. D., & Ostheimer, J. C. 2003, ApJ, 599, 1082
- Mandushev, G., Stancheva, A., & Spasova, N. 1991, A&A, 252, 94
- Mateo, M. L. 1998, ARA&A, 36, 435
- McMillan, P. J., & Binney, J. J. 2008, MNRAS, 390, 429
- McWilliam, A., Preston, G. W., Sneden, C., & Searle, L. 1995, AJ, 109, 2757
- McWilliam, A. 1997, ARA&A, 35, 503
- Newberg, H. J., et al. 2002, ApJ, 569, 245
- Nissen, P. E., & Schuster, W. J. 1997, A&A, 326, 751
- Odenkirchen, M., et al. 2001, ApJ, 548, L165
- Padmanabhan, N., et al. 2008, ApJ, 674, 1217
- Pier, J. R., Munn, J. A., Hindsley, R. B., Hennessy, G. S., Kent, S. M., Lupton, R. H., & Ivezić, Ž. 2003, AJ, 125, 1559
- Press, W. H., & Schechter, P. 1974, ApJ, 187, 425
- Prochaska, J. X., Naumov, S. O., Carney, B. W., McWilliam, A., & Wolfe, A. M. 2000, AJ, 120, 2513
- Purcell, C. W., Bullock, J. S., & Kazantzidis, S. 2010, MNRAS, 404, 1711
- Reddy, B. E., Tomkin, J., Lambert, D. L., & Allende Prieto, C. 2003, MNRAS, 340, 304
- Reddy, B. E., Lambert, D. L., & Allende Prieto, C. 2006, MNRAS, 367, 1329
- Robertson, B., Bullock, J. S., Font, A. S., Johnston, K. V., & Hernquist, L. 2005, ApJ, 632, 872
- Rocha-Pinto, H. J., Majewski, S. R., Skrutskie, M. F., Crane, J. D., & Patterson, R. J. 2004, ApJ, 615, 732

- Roederer, I. U. 2009, AJ, 137, 272
- Rocha-Pinto, H. J., Scalo, J., Maciel, W. J., & Flynn, C. 2000a, ApJ, 531, L115
- Rocha-Pinto, H. J., Scalo, J., Maciel, W. J., & Flynn, C. 2000b, A&A, 358, 869
- Rockosi, C. M., et al. 2002, AJ, 124, 349
- Ryan, S. G., & Norris, J. E. 1991a, AJ, 101, 1835
- Ryan, S. G., & Norris, J. E. 1991b, AJ, 101, 1865
- Scannapieco, E., & Bildsten, L. 2005, ApJ, 629, L85
- Schlaufman, K. C., et al. 2009, ApJ, 703, 2177
- Schönrich, R., & Binney, J. 2009a, MNRAS, 396, 203
- Schönrich, R., & Binney, J. 2009b, MNRAS, 399, 1145
- Seabroke, G. M., et al. 2008, MNRAS, 384, 11
- Smith, J. A., et al. 2002, AJ, 123, 2121
- Smith, M. C., et al. 2009, MNRAS, 399, 1223
- Sneden, C., Kraft, R. P., Shetrone, M. D., Smith, G. H., Langer, G. E., & Prosser, C. F. 1997, AJ, 114, 1964
- Sneden, C., Johnson, J., Kraft, R. P., Smith, G. H., Cowan, J. J., & Bolte, M. S. 2000a, ApJ, 536, L85
- Sneden, C., Pilachowski, C. A., & Kraft, R. P. 2000b, AJ, 120, 1351
- Springel, V., et al. 2005, Nature, 435, 629
- Starkenburg, E., et al. 2009, ApJ, 698, 567
- Stephens, A., & Boesgaard, A. M. 2002, AJ, 123, 1647
- Stewart, K. R., Bullock, J. S., Wechsler, R. H., Maller, A. H., & Zentner, A. R. 2008, ApJ, 683, 597
- Totten, E. J., & Irwin, M. J. 1998, MNRAS, 294, 1
- Totten, E. J., Irwin, M. J., & Whitelock, P. A. 2000, MNRAS, 314, 630
- Tucker, D. L., et al. 2006, Astronomische Nachrichten, 327, 821
- Venn, K. A., Irwin, M., Shetrone, M. D., Tout, C. A., Hill, V., & Tolstoy, E. 2004, AJ, 128, 1177
- Vivas, A. K., et al. 2001, ApJ, 554, L33
- Vivas, A. K., & Zinn, R. 2006, AJ, 132, 714
- Walker, M. G., Mateo, M., Olszewski, E. W., Peñarrubia, J., Wyn Evans, N., & Gilmore, G. 2009, ApJ, 704, 1274
- Watkins, L. L., et al. 2009, MNRAS, 398, 1757
- White, S. D. M., & Rees, M. J. 1978, MNRAS, 183, 341
- Yanny, B., et al. 2000, ApJ, 540, 825
- Yanny, B., et al. 2003, ApJ, 588, 824
- Yanny, B., et al. 2009, AJ, 137, 4377
- York, D. G., et al. 2000, AJ, 120, 1579
- Zoccali, M., Hill, V., Lecureur, A., Barbuy, B., Renzini, A., Minniti, D., Gómez, A., & Ortolani, S. 2008, A&A, 486, 177
- Zolotov, A., Willman, B., Brooks, A. M., Governato, F., Brook, C. B., Hogg, D. W., Quinn, T., & Stinson, G. 2009, ApJ, 702, 1058
- Zolotov, A., Willman, B., Brooks, A. M., Governato, F., Hogg, D. W., Shen, S., & Wadsley, J. 2010, ApJ, 721, 738

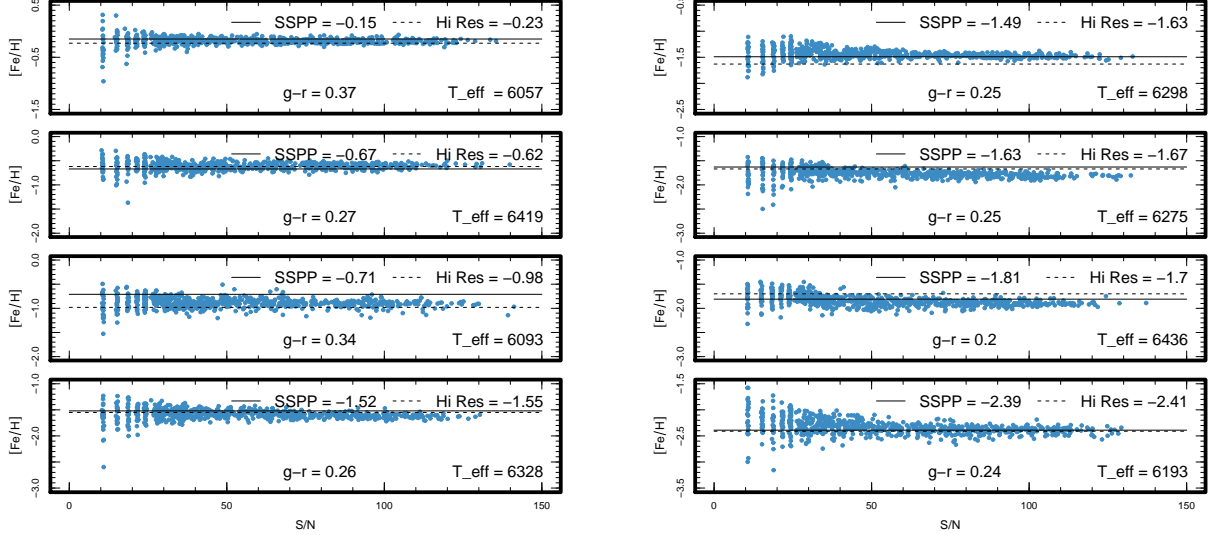


**Figure 1.** Ensemble of bootstrap coadd realizations of single MPMSTO stars giving SSPP [Fe/H] precision and accuracy as a function of S/N for that star. The [Fe/H] and  $T_{\text{eff}}$  estimates given for each star were derived from Hobby-Eberly Telescope High Resolution Spectrograph observations (Allende Prieto et al. 2008); we also include the SSPP [Fe/H] estimate for the original, single high S/N spectrum. Each point in the plot corresponds to the result of a SSPP analysis of a single bootstrap coadded spectrum made up of many model low S/N MPMSTO star spectra created by degrading a high S/N SEGUE MPMSTO star spectrum with a detailed noise model. The mean square error (MSE  $\equiv$  bias $^2$  + variance) of our SSPP analysis of coadded spectra ranges from 0.05 dex in [Fe/H] for the most iron-rich stars to 0.20 dex in [Fe/H] for the most iron-poor stars.

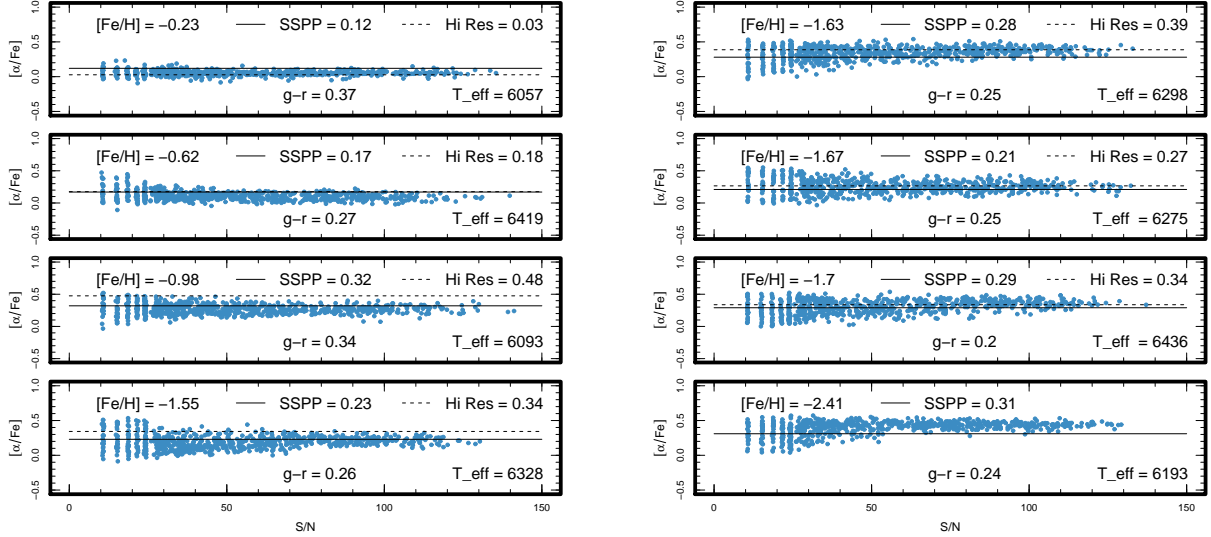


**Figure 2.** Ensemble of bootstrap coadd realizations of single MPMSTO stars giving SSPP  $[\alpha/\text{Fe}]$  precision and accuracy as a function of S/N for that star. The panels are in the same order as in Figure 1. The  $[\alpha/\text{Fe}]$  and  $T_{\text{eff}}$  estimates given for each star were derived from Hobby-Eberly Telescope High Resolution Spectrograph observations (Allende Prieto et al. 2008); we also include the SSPP  $[\alpha/\text{Fe}]$  estimate for the original, single high S/N spectrum. Each point in the plot corresponds to the result of a SSPP analysis of a single bootstrap coadded spectrum made up of many model low S/N MPMSTO star spectra created by degrading a high S/N SEGUE MPMSTO star spectrum with a detailed noise model. The MSE of our SSPP analysis of coadded spectra ranges from 0.05 dex in  $[\alpha/\text{Fe}]$  for the most iron-rich stars to 0.20 dex in  $[\alpha/\text{Fe}]$  for the most iron-poor stars.

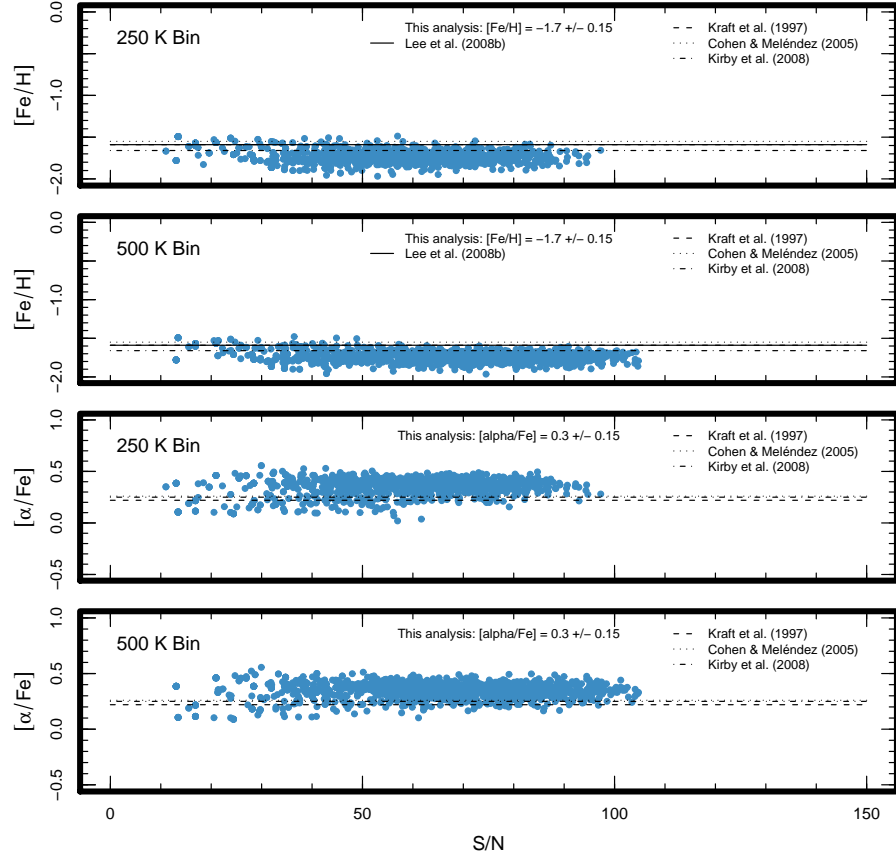


**Figure 3.** Ensemble of bootstrap coadd realizations of single MPMSTO stars giving SSPP  $[Fe/H]$  and  $[\alpha/Fe]$  precision and accuracy as a function of S/N for M 13. Each point in the plot corresponds to a single bootstrap coaddition of SEGUE MPMSTO spectra corresponding to stars with equatorial coordinates within the projected tidal radius of M 13, with radial velocities within  $15 \text{ km s}^{-1}$  of the systematic radial velocity of the cluster, and with  $g - r$  colors in an interval that corresponds to a range in effective temperature as noted in each panel. Note that the precision and accuracy of the SSPP analysis of the coadded spectra is not a strong function of the  $g - r$  color range (and therefore  $T_{\text{eff}}$  range) of the MPMSTO stars included in the coadd. Combined with the fact that coadding in 500 K bins always leads to a higher S/N coadded spectrum, we coadd spectra corresponding to MPMSTO stars in the bin of  $g - r$  color corresponding to the  $T_{\text{eff}}$  bin of width 500 K centered on the  $T_{\text{eff}}$  value that gives the highest S/N in the resultant coadded spectrum. In this way, the SSPP produces an estimate for the metallicity of M 13 of  $[Fe/H] = -1.7 \pm 0.15$  and  $[\alpha/Fe] = 0.3 \pm 0.15$  in rough agreement with previous analyses (Kraft et al. 1997; Cohen & Meléndez 2005; Kirby et al. 2008a).

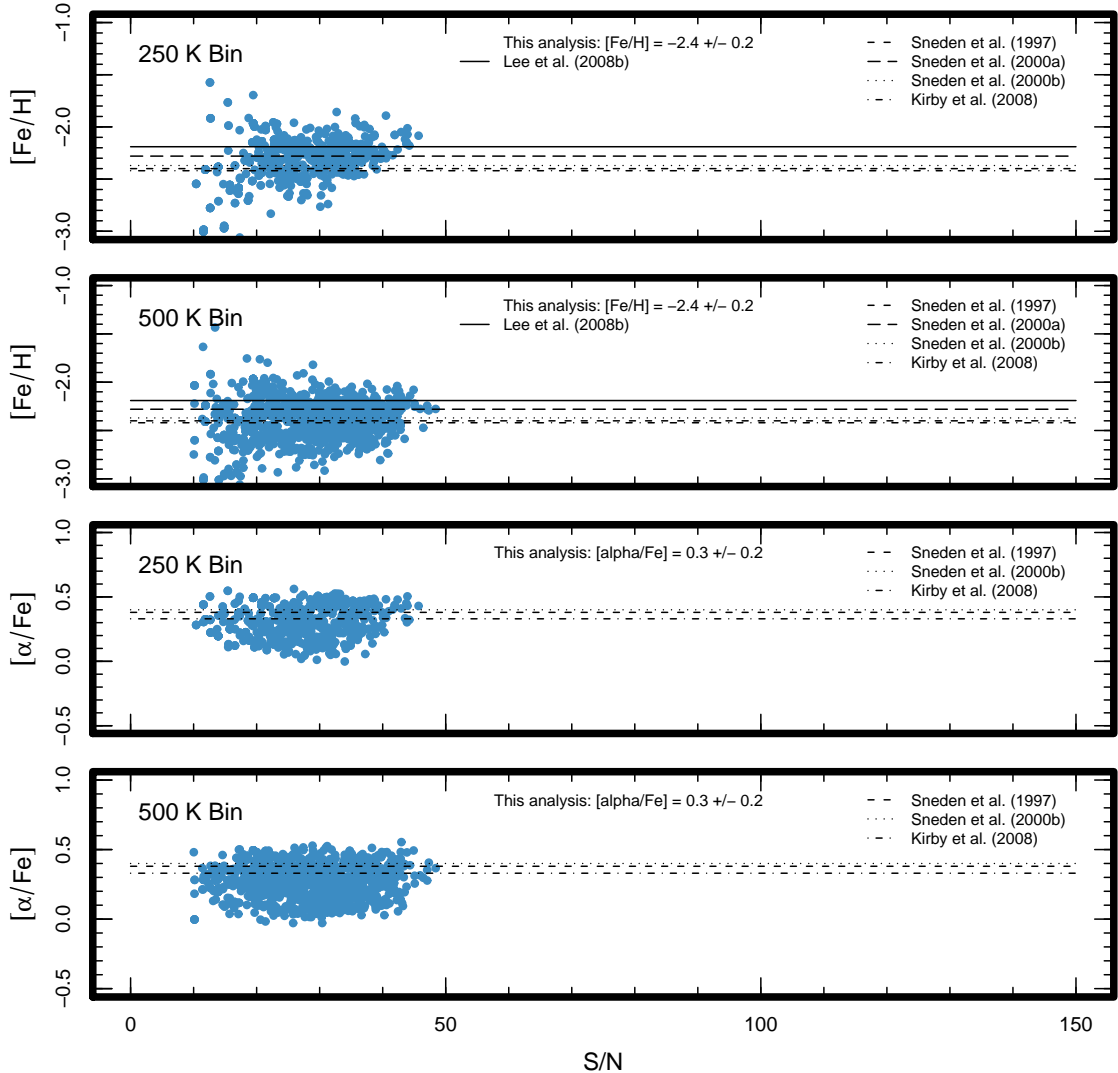


**Figure 4.** Ensemble of bootstrap coadd realizations of single MPMSTO stars giving SSPP  $[\text{Fe}/\text{H}]$  and  $[\alpha/\text{Fe}]$  precision and accuracy as a function of S/N for M 15. Each point in the plot corresponds to a single bootstrap coaddition of SEGUE MPMSTO spectra corresponding to stars with equatorial coordinates within the projected tidal radius of M 15, with radial velocities within  $25 \text{ km s}^{-1}$  of the systematic radial velocity of the cluster, and with  $g - r$  colors in an interval that corresponds to a range in effective temperature as noted in each panel. In this way, the SSPP produces an estimate for the metallicity of M 15 of  $[\text{Fe}/\text{H}] = -2.4 \pm 0.2$  and  $[\alpha/\text{Fe}] = 0.3 \pm 0.2$  in rough agreement with previous analyses (Sneden et al. 1997, 2000a,b; Kirby et al. 2008a).

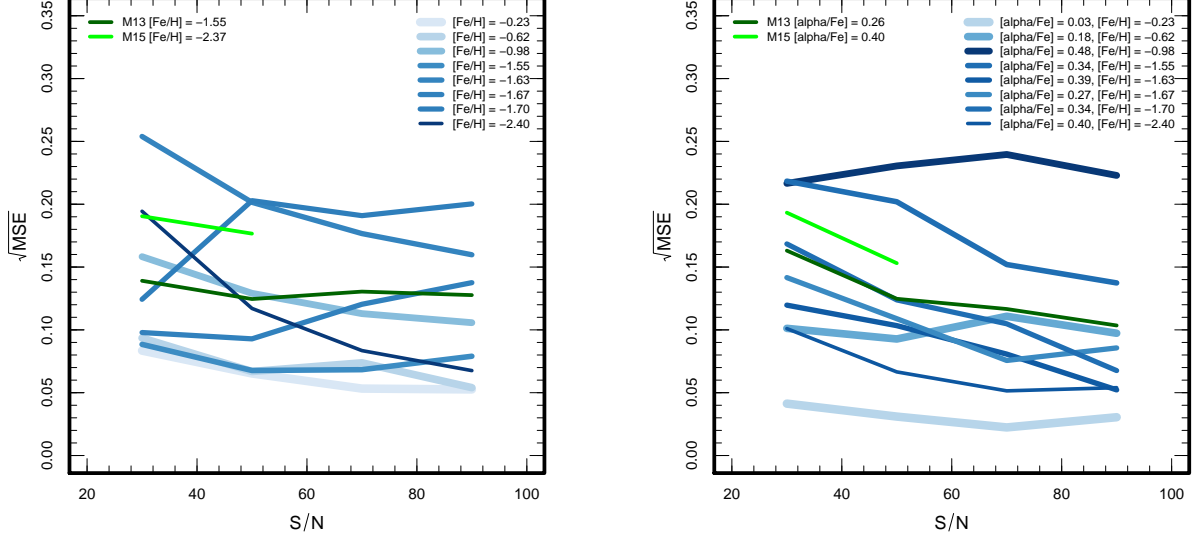


**Figure 5.** The mean square error ( $MSE \equiv \text{bias}^2 + \text{variance}$ ) of our SSPP analysis of coadded MPMSTO spectra as a function of S/N and metallicity. The blue curves correspond to our analysis of the noise-added spectra, while the green curves correspond to our analysis for M 13 and M 15. The widths of the curves are common between both panels in that the curve for a single star is plotted with the same width in both panels. In both panels, the most solar-like compositions are always the lightest shades of blue. Note that the SSPP produces more precise  $[\text{Fe}/\text{H}]$  and  $[\alpha/\text{Fe}]$  estimates at common S/N for the most metal-rich MPMSTO stars. In that case, the abundance of metal lines in the moderate resolution SEGUE spectra of metal-rich stars permits precise  $[\text{Fe}/\text{H}]$  estimates. Also note that the MSE of our analysis is more strongly affected by population metallicity than it is affected by the coaddition of MPMSTO star spectra with a small but finite range of  $T_{\text{eff}}$  and  $\log g$ . For that reason, the expected MSE of our analysis is best determined by our analysis of the noise-added spectra. Ultimately, including both statistical and systematic effects, our SSPP analysis of coadded SEGUE MPMSTO spectra produces estimates that are precise and accurate enough to identify differences on the order of 0.2 dex in both  $[\text{Fe}/\text{H}]$  and  $[\alpha/\text{Fe}]$ . *Left:* SSPP  $[\text{Fe}/\text{H}]$  MSE as a function of S/N and metallicity. *Right:* SSPP  $[\alpha/\text{Fe}]$  MSE as a function of S/N and metallicity.

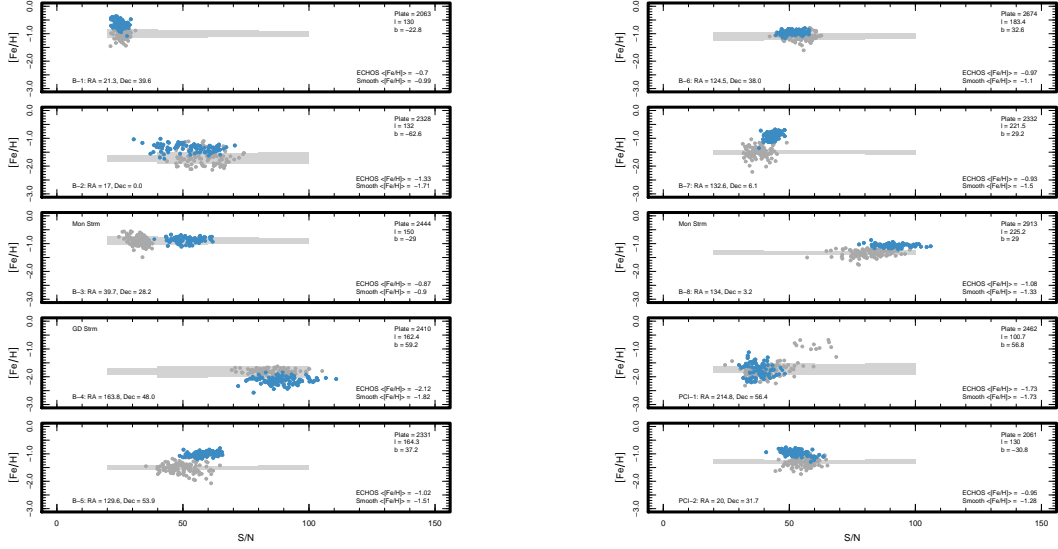


**Figure 6.** Ensemble of bootstrap coadd realizations giving SSPP [Fe/H] estimates for ECHOS from S09 using bootstrap coaddition of individual SEGUE MPMSTO star spectra. Each blue point corresponds to a SSPP [Fe/H] estimate for a single ECHOS bootstrap coadd, while the dark gray points are SSPP [Fe/H] estimates from an equivalent bootstrap coaddition of MPMSTO star spectra with radial velocities indicating membership in the kinematically smooth inner halo MPMSTO population along the same SEGUE line of sight that hosts the ECHOS. MPMSTO stars correspond to an ECHOS if they have a radial velocity consistent with radial velocity overdensities as determined by S09; we identify all other stars along the same line of sight as the kinematically smooth inner halo MPMSTO population. Of those MPMSTO stars that are radial velocity members of an ECHOS, we include in the coadd only those spectra that correspond to stars that have  $g - r$  colors corresponding to the  $T_{\text{eff}}$  bin of width 500 K centered on the  $T_{\text{eff}}$  value that gives the highest S/N in the resultant coadded spectrum. In the same way, we choose an optimal  $T_{\text{eff}}$  bin of width 500 K from which we select spectra for coaddition from the kinematically smooth inner halo MPMSTO population. The light gray polygon is centered on the mean metallicity of the smooth component of the inner halo along each SEGUE line of sight and indicates the expected MSE of the SSPP at the metallicity of the smooth component as a function of S/N from our bootstrap coaddition of high S/N spectra degraded with the noise model (see Figure 5). Therefore, if the cloud of blue points does not coincide with the gray polygon, then the ECHOS is chemically distinct from the kinematically smooth population along that line of sight. In all cases where the quoted metallicity of the smooth component is more iron-rich than typically associated with the smooth inner halo, the reason is because the ECHOS dominates the MPMSTO population along that line of sight (see Figures 2 through 11 of S09). *Left:* SSPP [Fe/H] analysis for ECHOS B-1, B-2, B-3 (Monoceros), B-4 (Grillmair & Dionatos 2006), and B-5 from Table 1. *Right:* SSPP [Fe/H] analysis for ECHOS B-6, B-7, and B-8 from Table 1 as well as PCI-1 and PCI-2 from Table 2.

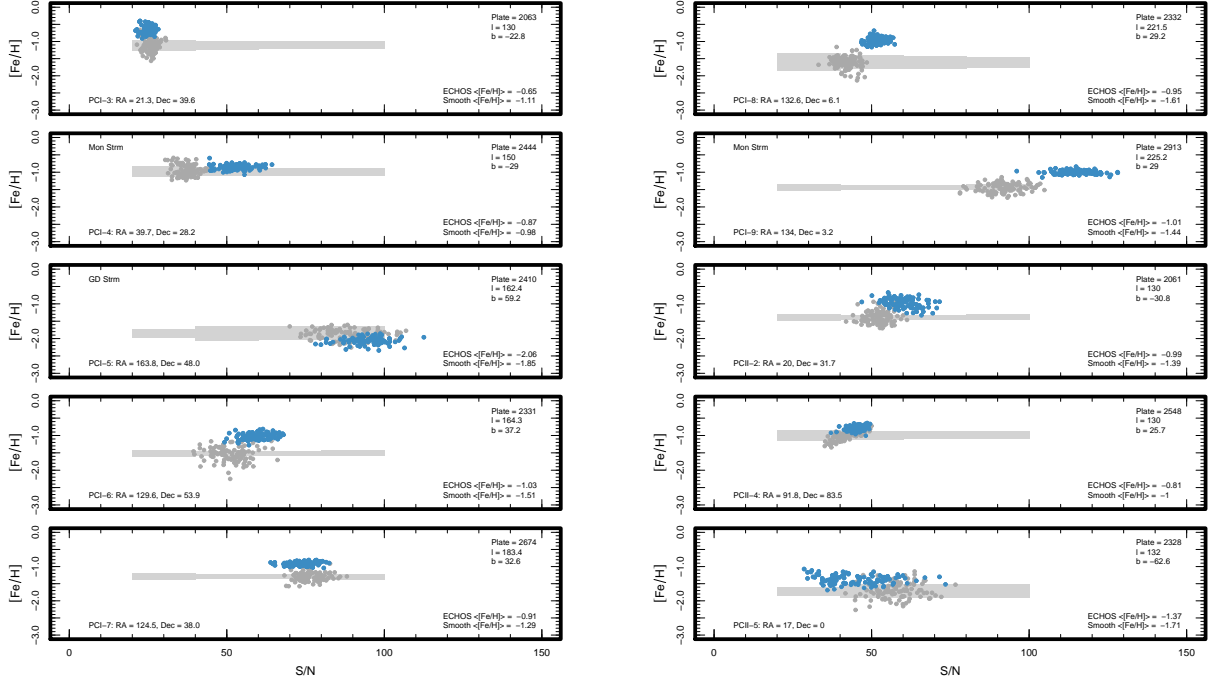


**Figure 7.** *Left:* SSPP [Fe/H] analysis for ECHOS PCI-3, PCI-4 (Monoceros), PCI-5 (Grillmair & Dionatos 2006), PCI-6, and PCI-7 from Table 2. *Right:* SSPP [Fe/H] analysis for ECHOS PCI-8 and PCI-9 (Monoceros) from Table 2 as well as PCII-2, PCII-4, and PCII-5 from Table 3. See the caption to Figure 6 for a detailed description of this type of figure.

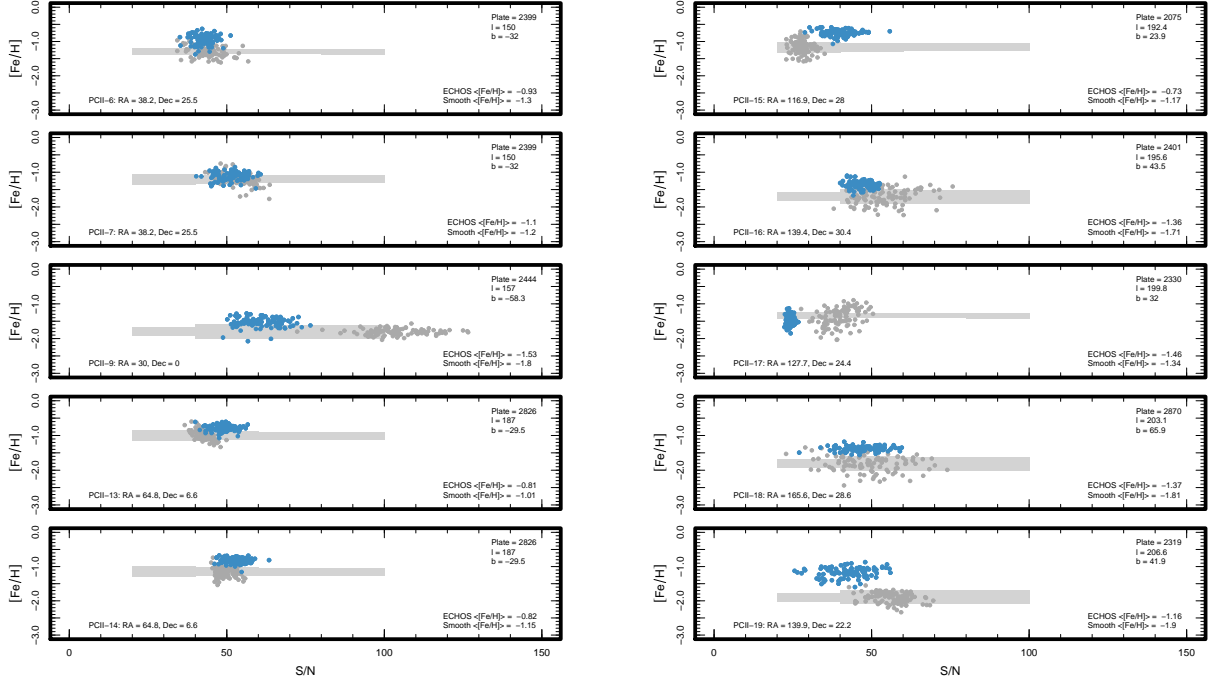


**Figure 8.** Left: SSPP [Fe/H] analysis for ECHOS PCII-6, PCII-7, PCII-9, PCII-13, and PCII-14 from Table 3. Right: SSPP [Fe/H] analysis for ECHOS PCII-15, PCII-16, PCII-17, PCII-18, PCII-19 from Table 3. See the caption to Figure 6 for a detailed description of this type of figure.

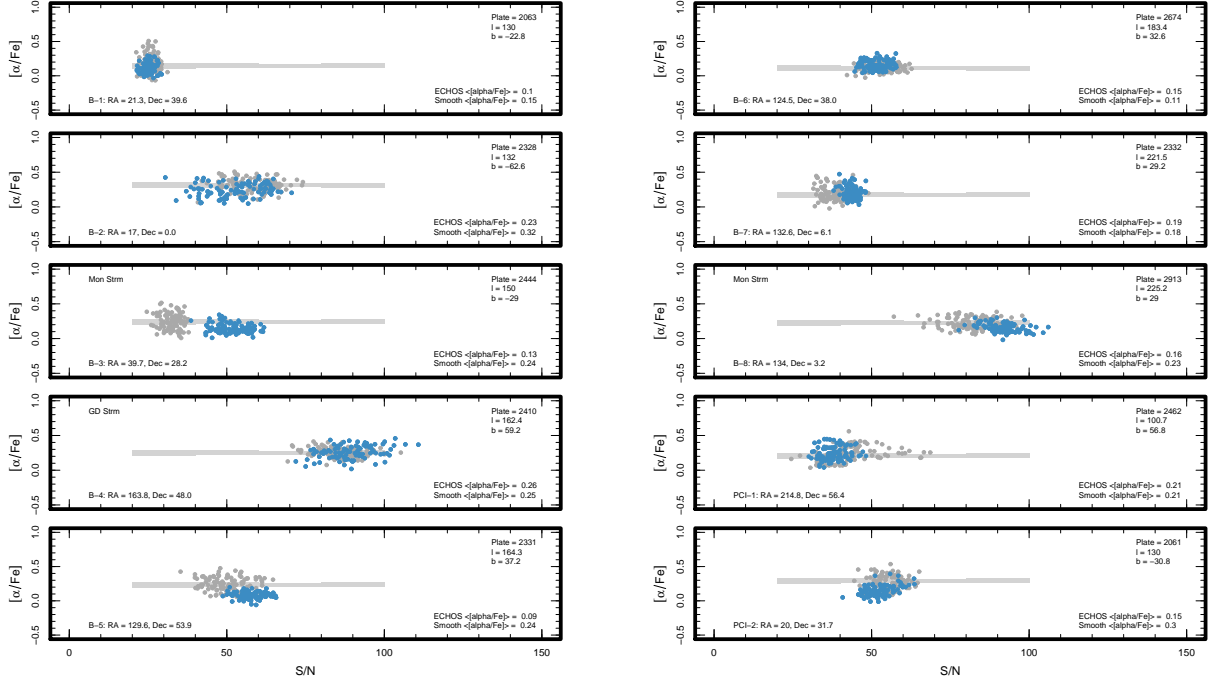


**Figure 9.** SSPP  $[\alpha/\text{Fe}]$  estimates for ECHOS from S09 using bootstrap coaddition of SEGUE MPMSTO star spectra. *Left:* SSPP  $[\alpha/\text{Fe}]$  analysis for ECHOS B-1, B-2, B-3 (Monoceros), B-4 (Grillmair & Dionatos 2006), and B-5 from Table 1. *Right:* SSPP  $[\alpha/\text{Fe}]$  analysis for ECHOS B-6, B-7, and B-8 from Table 1 as well as PCI-1 and PCI-2 from Table 2. See the caption to Figure 6 for a detailed description of this type of figure.

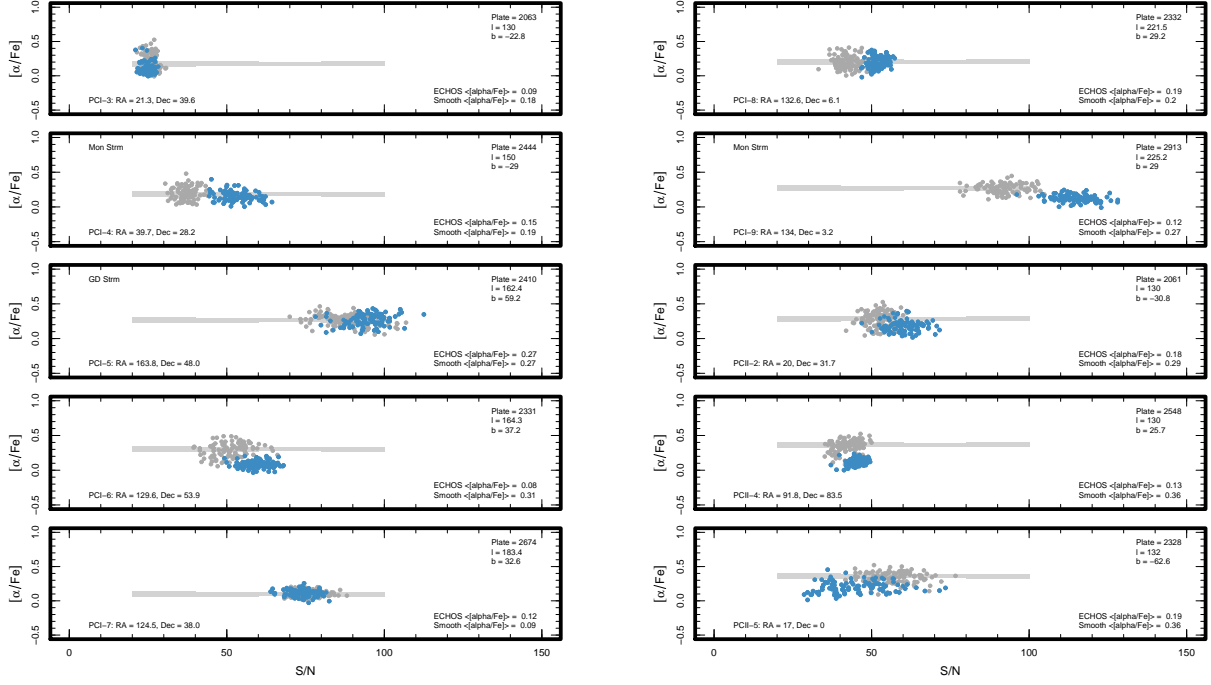


**Figure 10.** *Left:* SSPP  $[\alpha/\text{Fe}]$  analysis for ECHOS PCI-3, PCI-4 (Monoceros), PCI-5 (Grillmair & Dionatos 2006), PCI-6, and PCI-7 from Table 2. *Right:* SSPP  $[\alpha/\text{Fe}]$  analysis for ECHOS PCI-8 and PCI-9 (Monoceros) from Table 2 as well as PCII-2, PCII-4, and PCII-5 from Table 3. See the caption to Figure 6 for a detailed description of this type of figure.

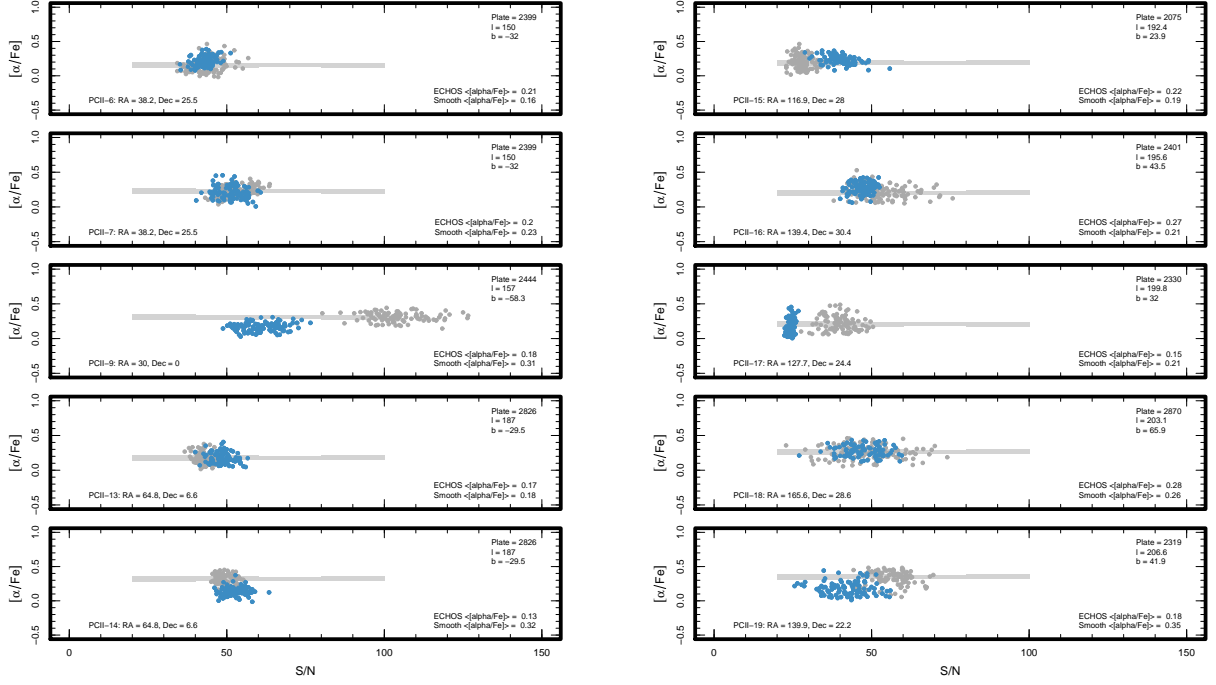


**Figure 11.** *Left:* SSPP  $[\alpha/\text{Fe}]$  analysis for ECHOS PCII-6, PCII-7, PCII-9, PCII-13, and PCII-14 from Table 3. *Right:* SSPP  $[\alpha/\text{Fe}]$  analysis for ECHOS PCII-15, PCII-16, PCII-17, PCII-18, PCII-19 from Table 3. See the caption to Figure 6 for a detailed description of this type of figure.

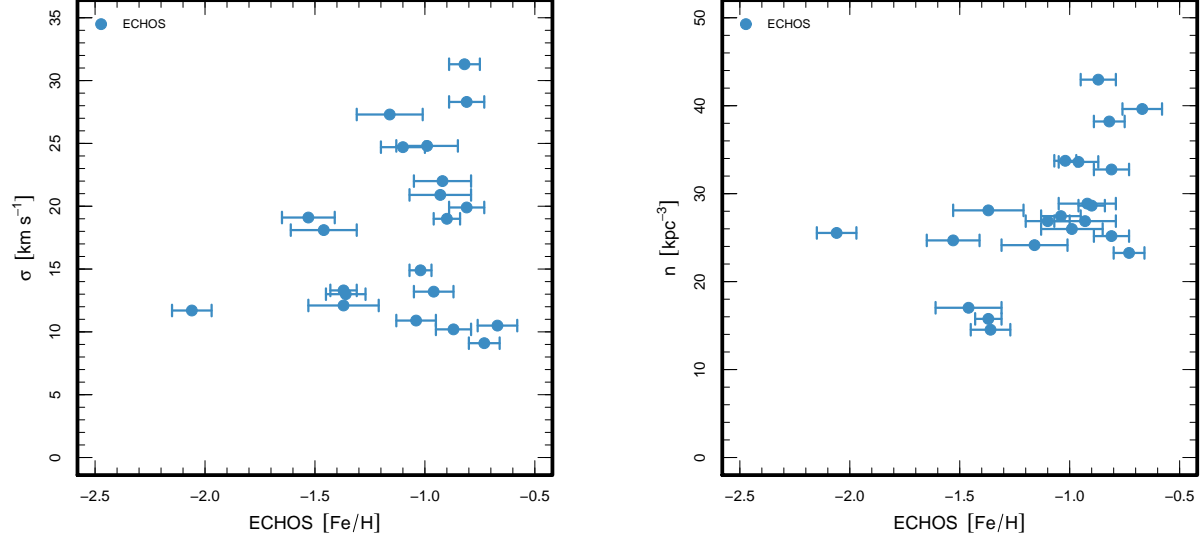


**Figure 12.** Kinematic properties of ECHOS as a function of metallicity. *Left:* Iron-rich ECHOS can have large velocity dispersions. *Right:* Iron-rich ECHOS have the highest space densities; this prominence of metal-rich substructures was predicted in Font et al. (2006).

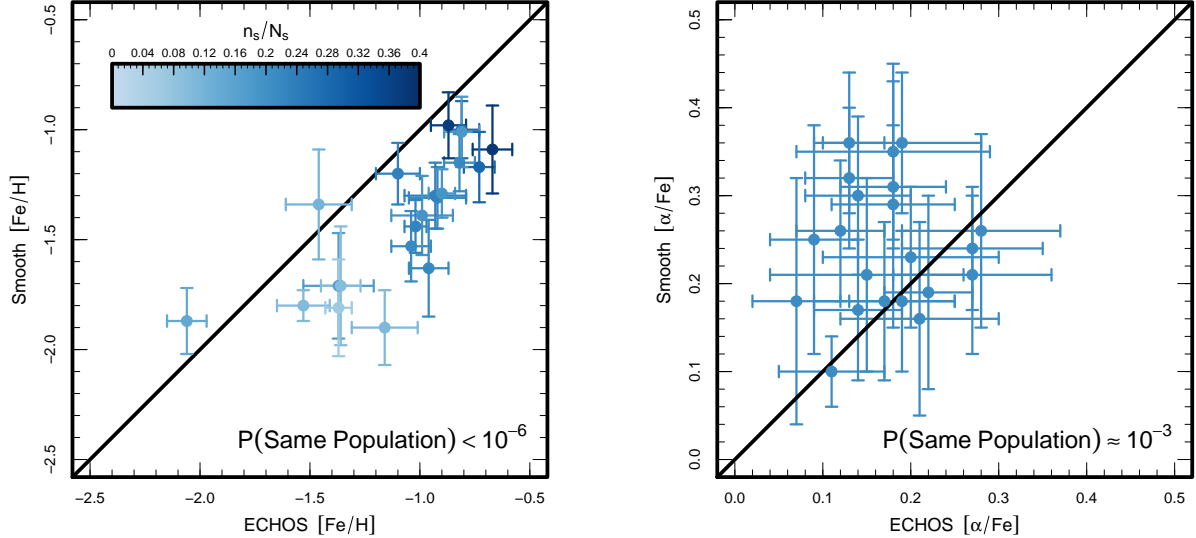


**Figure 13.** Comparison of the metallicity of ECHOS to the metallicity of the MPMSTO population in the kinematically smooth component of the inner halo along the same line of sight where the ECHOS was discovered. *Left:* ECHOS are more iron-rich than the MPMSTO stars associated with the kinematically smooth inner halo. Moreover, ECHOS are so iron-rich that an origin within one or more now tidally disrupted ultrafaint dwarf galaxies is unlikely. That is, the mass–luminosity relation of Milky Way dwarf spheroidal galaxies (e.g., Kirby et al. 2008b) requires a progenitor luminosity  $L \sim 10^8 L_\odot$  to reach a mean iron metallicity  $[\text{Fe}/\text{H}] \sim -1.0$ . Lines of sight hosting an ECHOS for which we infer a smooth component metallicity  $[\text{Fe}/\text{H}] \gtrsim -1.6$  are those lines of sight along which the ratio of the number of MPMSTO stars with radial velocities consistent with ECHOS membership  $n_s$  to the total number of MPMSTO stars with radial velocity measurements  $N_s$  is non-negligible, or  $n_s/N_s \gtrsim 0$ . In other words, lines of sight where ECHOS are a significant contributor to the MPMSTO population tend to have inferred smooth component metallicities  $[\text{Fe}/\text{H}] \gtrsim -1.6$ . As a result, those apparently enhanced iron metallicities in the smooth component are likely due to the presence of stars that are outside the radial velocity overdensity that defines the ECHOS, but that are still associated with ECHOS. *Right:* ECHOS are less  $\alpha$ -enhanced than the MPMSTO stars associated with the kinematically smooth inner halo, so (modulo any changes in the initial mass function) the MPMSTO stars in ECHOS formed in environments in which the star formation timescale was long relative to the star formation timescale in the massive progenitor of the bulk of the inner halo (e.g., Robertson et al. 2005).

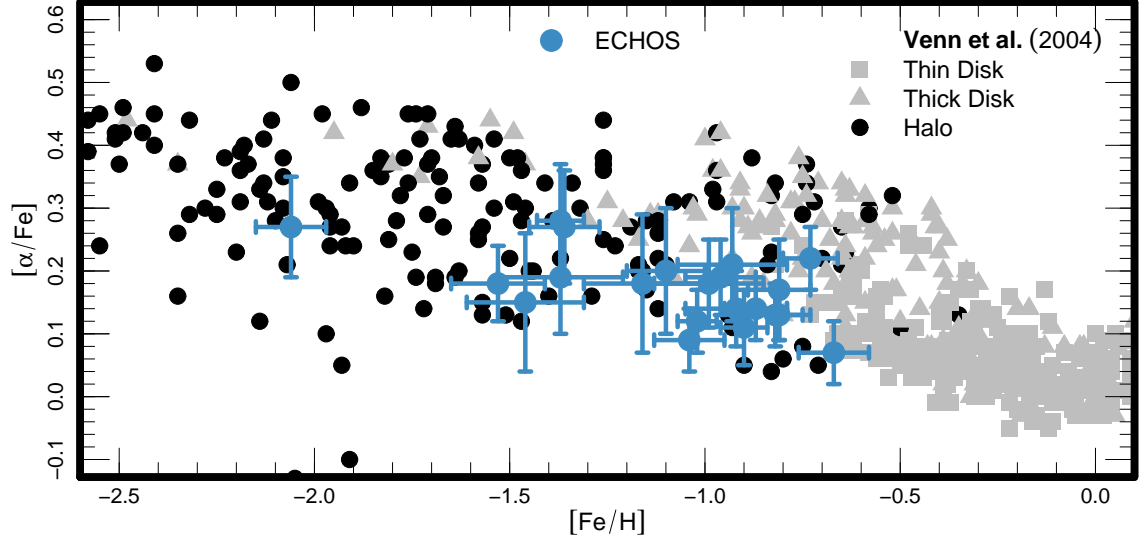


**Figure 14.** Distribution of ECHOS in the  $[\text{Fe}/\text{H}]$ - $[\alpha/\text{Fe}]$  plane along with individual stars collected from the literature as presented in Venn et al. (2004). The ECHOS mostly fall in a region of that plane that is relatively sparsely occupied by—but not completely barren of—individual stars. In general, the ECHOS are more iron-poor than thick-disk stars and more iron-poor and  $\alpha$ -enhanced than typical thin-disk stars.

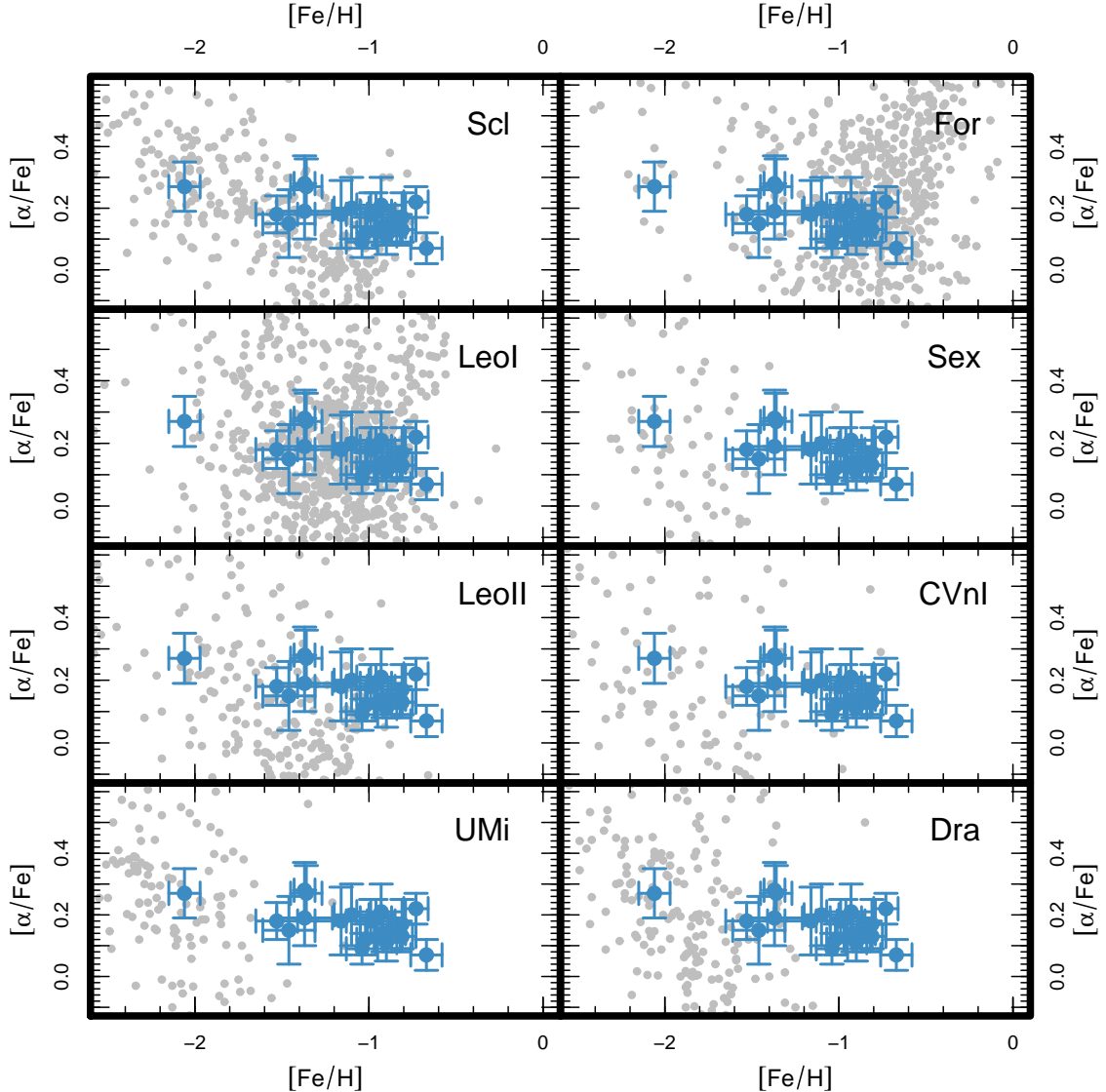


**Figure 15.** Distribution of ECHOS in the  $[\text{Fe}/\text{H}]$ - $[\alpha/\text{Fe}]$  plane along with individual stars in dSph galaxies from Kirby et al. (2010). In each panel, the gray points in the background represent  $[\text{Fe}/\text{H}]$  and  $[\alpha/\text{Fe}]$  measurements for individual dSph stars. The blue points in the foreground are our  $[\text{Fe}/\text{H}]$  and  $[\alpha/\text{Fe}]$  measurements for individual ECHOS. Left to right and top to bottom, the dSph galaxies are: Sculptor, Fornax, Leo I, Sextans, Leo II, Canes Venatici I, Ursa Minor, and Draco. ECHOS are plausibly associated with a progenitor comparable to Sculptor or Leo I.

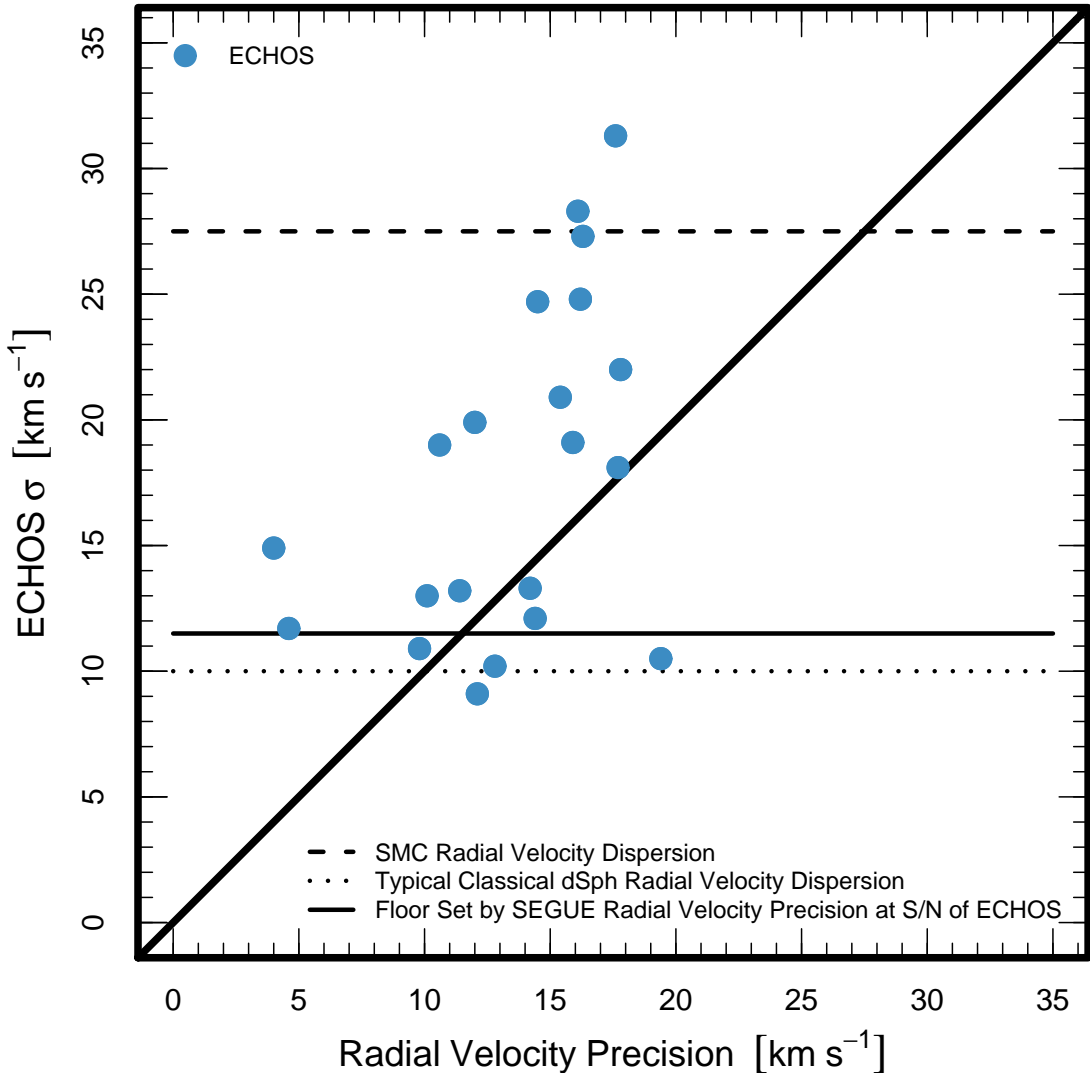


**Figure 16.** Velocity dispersion of ECHOS as a function of the median radial velocity precision of the stars in the ECHOS. The fact that the points are above the line  $y = x$  suggests that the observed velocity dispersion is not only a function of the limited radial velocity precision for faint MPMSTO stars. The velocity dispersion observed in an ECHOS is a lower limit on the velocity dispersion of any gravitationally bound progenitor. This results from the fact that the phase-space distribution of a disrupted stellar system becomes colder with time, combined with the fact that each SEGUE line of sight would only intersect a small fraction of an orbit of an element of halo substructure. Typical classical dwarf spheroidal galaxies have radial velocity dispersions  $\sigma \sim 10 \text{ km s}^{-1}$  (e.g., Mateo 1998), while the SMC has a velocity dispersion of  $\sigma \approx 27.5 \pm 0.5 \text{ km s}^{-1}$  (e.g., Harris & Zaritsky 2006). The origin of ECHOS through the gravitational disruption of a progenitor with a velocity dispersion  $\sigma > 20 \text{ km s}^{-1}$  implies a progenitor mass  $M_{\text{tot}} \gtrsim 10^9 M_{\odot}$ .

**Table 1**  
Properties of ECHOS

ID	RA (deg)	Dec (deg)	l (deg)	b (deg)	bplate	fplate	N <sub>s</sub>	N <sub>p</sub>	Vol (kpc <sup>3</sup> )	d (kpc)	err (kpc)	v <sub>r</sub> (km s <sup>-1</sup> )	n <sub>s</sub>	[Fe/H] <sub>E</sub> (dex)	err (dex)	[Fe/H] <sub>S</sub> (dex)	err (dex)	[α] (dex)
B-1	21.3	39.6	130.0	-22.8	2043	2063	34	228	2.20	18.4	3.2	-130	12	-0.70	0.12	-0.99	0.18	
B-2	17.0	0.0	132.0	-62.6	2313	2328	109	561	3.48	10.8	6.6	-170	20	-1.33	0.14	-1.71	0.25	
B-3 <sup>a</sup>	39.7	28.2	150.0	-29.0	2442	2444	59	265	2.30	11.2	2.0	-50	17	-0.87	0.09	-0.90	0.15	
B-4 <sup>b</sup>	163.8	48.0	162.4	59.2	2390	2410	150	672	3.86	6.6	2.8	-130	25	-2.12	0.11	-1.82	0.13	
B-5	129.6	53.9	164.3	37.2	2316	2331	93	425	3.33	9.6	2.5	-10	20	-1.02	0.09	-1.51	0.17	
B-6	124.5	38.0	183.4	32.6	2670	2674	83	514	3.46	9.9	1.1	30	17	-0.97	0.06	-1.10	0.13	
B-7	132.6	6.1	221.5	29.2	2317	2332	69	470	3.04	11.0	1.3	70	17	-0.93	0.10	-1.50	0.18	
B-8 <sup>a</sup>	134.0	3.2	225.2	29.0	2888	2913	74	514	3.50	11.0	1.7	90	19	-1.08	0.05	-1.33	0.14	

**Note.** — Kinematic and metallicity data for all bin detection ECHOS from S09. The columns are: right ascension, declination, galactic longitude, plate number, SEGUE faint plate number, number of SEGUE MPMSTO spectra along the indicated line of sight, number of photometric MPMSTO spectra along the indicated line of sight, volume scanned along the indicated line of sight, median distance of the stars in the ECHOS, the error in that estimate, the radial velocity of the stars in the ECHOS, the number of stars in the ECHOS, the error in that estimate, the iron metallicity of the stars in the ECHOS, the error in that estimate, the iron metallicity of the stars kinematically associated with the ECHOS, the error in that estimate, the α-enhancement of the stars in the ECHOS, the error in that estimate, the iron metallicity of the stars in the halo along the indicated line of sight, the error in that estimate, the α-enhancement of the stars in the halo along the indicated line of sight, the error in that estimate, the iron metallicity of the halo along the indicated line of sight, the error in that estimate, the α-enhancement of the halo along the indicated line of sight, and the error in that estimate.

<sup>a</sup> Monoceros Stream

<sup>b</sup> Grillmair & Dionatos (2006) Stream

**Table 2**  
Properties of ECHOS

ID	RA (deg)	Dec (deg)	l (deg)	b (deg)	bplate	fplate	N <sub>s</sub>	N <sub>p</sub>	Vol (kpc <sup>3</sup> )	d (kpc)	err (kpc)	v <sub>r</sub> (km s <sup>-1</sup> )	σ (km s <sup>-1</sup> )	err (km s <sup>-1</sup> )	n <sub>s</sub>	[Fe/H] <sub>E</sub> (dex)	e (dex)
PCI-1	214.8	56.4	100.7	56.8	2447	2462	122	673	2.79	8.7	2.3	-328	15.1	11.5	8	-1.73	0
PCI-2	20.0	31.7	130.0	-30.8	2041	2061	93	349	2.60	13.4	3.3	-125	22.0	17.8	20	-0.95	0
PCI-3	21.3	39.6	130.0	-22.8	2043	2063	34	228	2.20	18.7	3.5	-121	10.5	19.4	13	-0.65	0
PCI-4 <sup>a</sup>	39.7	28.2	150.0	-29.0	2442	2444	59	265	2.30	11.4	2.6	-57	10.2	12.8	22	-0.87	0
PCI-5 <sup>b</sup>	163.8	48.0	162.4	59.2	2930	2410	150	672	3.86	6.6	2.5	-132	11.7	4.6	22	-2.06	0
PCI-6	129.6	53.9	164.3	37.2	2316	2331	93	425	3.33	10.0	2.4	-13	10.9	9.8	20	-1.03	0
PCI-7	124.5	38.0	183.4	32.6	2670	2674	83	514	3.46	10.1	1.5	29	19.0	10.6	16	-0.91	0
PCI-8	132.6	6.1	221.5	29.2	2317	2332	69	470	3.04	10.9	1.6	71	13.2	11.4	15	-0.95	0
PCI-9 <sup>a</sup>	134.0	3.2	225.2	29.0	2888	2913	74	514	3.50	10.3	1.4	85	14.9	4.0	17	-1.01	0

**Note.** — Kinematic and metallicity data for all class I peak detection ECHOS from S09. The columns are: right ascension, declination, galactic l, b, SEGUE faint plate number, number of SEGUE MPMSTO spectra along the indicated line of sight, number of photometric MPMSTO candidates along the indicated line of sight, median distance of the stars in the ECHOS, the error in that estimate, the radial velocity of the ECHOS, the velocity dispersion of stars in the ECHOS, the number of MPMSTO stars kinematically associated with the ECHOS, the iron metallicity of the ECHOS, the error in that component of the halo along the indicated line of sight, the error in that estimate, the  $\alpha$ -enhancement of the ECHOS, the error in that estimate, the error in the halo along the indicated line of sight, and the error in that estimate.

<sup>a</sup> Monoceros Stream

<sup>b</sup> Grillmair & Dionatos (2006) Stream

**Table 3**  
Properties of ECHOS

ID	RA (deg)	Dec (deg)	l (deg)	b (deg)	bplate	fplate	N <sub>s</sub>	N <sub>p</sub>	Vol (kpc <sup>3</sup> )	d (kpc)	err (kpc)	v <sub>r</sub> (km s <sup>-1</sup> )	σ (km s <sup>-1</sup> )	err (km s <sup>-1</sup> )	n <sub>s</sub>	[Fe/H] <sub>E</sub> (dex)	α
PCII-1	20.0	31.7	130.0	-30.8	2041	2061	93	349	2.60	13.4	3.3	-125	22.0	17.8	20	-0.92	
PCII-2	20.0	31.7	130.0	-30.8	2041	2061	93	349	2.60	12.7	3.4	-98	24.8	16.2	18	-0.99	
PCII-3	21.3	39.6	130.0	-22.8	2043	2063	34	228	2.20	18.7	3.5	-121	10.5	19.4	13	-0.67	
PCII-4	91.8	83.5	130.0	25.7	2540	2548	47	223	2.45	12.7	1.9	-95	19.9	12.0	13	-0.81	
PCII-5	17.0	0.0	132.0	-62.6	2313	2328	109	561	3.48	12.0	6.1	-173	12.1	14.4	19	-1.37	
PCII-6	38.2	25.5	150.0	-32.0	2379	2399	60	273	2.37	11.6	2.7	-93	20.9	15.4	14	-0.93	
PCII-7	38.2	25.5	150.0	-32.0	2379	2399	60	273	2.37	11.0	2.3	-66	24.7	14.5	14	-1.10	
PCII-8 <sup>a</sup>	39.7	28.2	150.0	-29.0	2045	2065	59	265	2.30	13.9	6.8	-57	10.2	12.8	22	-0.87	
PCII-9	30.0	0.0	157.0	-58.3	2442	2444	173	987	4.16	10.1	2.4	-177	19.1	15.9	18	-1.53	
PCII-10 <sup>b</sup>	163.8	48.0	162.4	59.2	2390	2410	150	672	3.86	6.6	2.5	-132	11.7	4.6	22	-2.06	
PCII-11	129.6	53.9	164.3	37.2	2316	2331	93	425	3.33	10.0	2.4	-13	10.9	9.8	20	-1.04	
PCII-12	124.5	38.0	183.4	32.6	2670	2674	83	514	3.46	10.1	1.5	29	19.0	10.6	16	-0.90	
PCII-13	64.8	6.6	187.0	-29.5	2805	2826	65	353	1.99	11.9	1.9	20	28.3	16.1	12	-0.81	
PCII-14	64.8	6.6	187.0	-29.5	2805	2826	65	353	1.99	12.3	1.7	44	31.3	17.6	14	-0.82	
PCII-15	116.9	28.0	192.4	23.9	2055	2075	35	254	3.12	14.3	1.1	44	9.1	12.1	10	-0.73	
PCII-16	139.4	30.4	195.6	43.5	2381	2401	114	527	3.50	7.6	2.0	-103	13.0	10.1	11	-1.36	
PCII-17	127.7	24.4	199.8	32.0	2315	2330	83	431	3.05	12.5	2.5	-40	18.1	17.7	10	-1.46	
PCII-18	165.6	28.6	203.1	65.9	2855	2870	151	764	3.21	8.6	4.7	-157	13.3	14.2	10	-1.37	
PCII-19	139.9	22.2	206.6	41.9	2304	2319	102	609	2.72	14.5	3.4	-55	27.3	16.3	11	-1.16	
PCII-20	132.6	6.1	221.5	29.2	2317	2332	69	470	3.04	10.9	1.6	71	13.2	11.4	15	-0.96	
PCII-21 <sup>a</sup>	134.0	3.2	225.2	29.0	2888	2913	74	514	3.50	10.3	1.4	85	14.9	4.0	17	-1.02	

**Note.** — Kinematic and metallicity data for all class II peak detection ECHOS from S09. The columns are: right ascension, declination, galactic SEGUE faint plate number, number of SEGUE MPMSTO spectra along the indicated line of sight, number of photometric MPMSTO candidates along the line of sight, median distance of the stars in the ECHOS, the error in that estimate, the radial velocity of the ECHOS, the velocity dispersion of the ECHOS, the number of MPMSTO stars kinematically associated with the ECHOS, the iron metallicity of the ECHOS, the error in that estimate, the halo along the indicated line of sight, the error in that estimate, the  $\alpha$ -enhancement of the ECHOS, the error in that estimate, the  $\alpha$ -enhancement of the indicated line of sight, and the error in that estimate.

<sup>a</sup> Monoceros Stream

<sup>b</sup> Grillmair & Dionatos (2006) Stream